



Validation Activities of Aeolus Wind Products in the Southeastern Iberian Peninsula

Jesús Abril-Gago^{1,2}, Pablo Ortiz-Amezcu³, Diego Bermejo-Pantaleón^{1,2}, Juana Andújar-Maqueda^{1,2}, Juan Antonio Bravo-Aranda^{1,2}, María José Granados-Muñoz^{1,2}, Francisco Navas-Guzmán^{1,2}, Lucas Alados-Arboledas^{1,2}, Inmaculada Foyo-Moreno^{1,2}, Juan Luis Guerrero-Rascado^{1,2}

¹Andalusian Institute for Earth System Research (IISTA-CEAMA), Granada, 18006, Spain.

²Applied Physics Department, University of Granada, Granada, 18071, Spain.

³Faculty of Physics, University of Warsaw, Warsaw, 02-093, Poland.

Correspondence to: Juan Luis Guerrero-Rascado (rascado@ugr.es)

Abstract. A statistical validation campaign of Aeolus L2B wind products has been performed with a ground-based Doppler lidar system and radiosondes at the ACTRIS/AGORA facility in Granada (Spain). The validation activities with the automatic ground-based lidar system lasted from the release of the reprocessed Aeolus data to the orbit shift of June 2021. This validation was performed using 109 B10 and B11 Aeolus products (within 100 km around the station) and 30-min averages of coincident ground-based lidar measurements (mean bin distance of ~50 km). The comparison yielded an approximately equal overestimation and underestimation of Aeolus HLOS wind speed during that period for the Rayleigh clear and Mie cloudy configurations. However, the reliability of the results was constrained to Aeolus' lowermost bins (roughly up to 3.5 km asl), due to the limited vertical coverage of the ground-based lidar measurements. Several spin-off analyses were performed varying the maximum distance to consider an Aeolus bin into the comparison and the average of the ground-based lidar measurements, in order to confirm the reliability of the criteria considered. An additional study was performed with Aeolus products after the orbit shift (B12 with a mean bin distance of ~75 km). A set of 7 radiosondes were launched between June 2021 and July 2022 (B12, mean bin distance of ~75 km) aiming to increase their coincidence in space and time with the satellite overpass (~30 minutes before). The radiosondes could provide full vertical coverage of Aeolus profiles (from surface up to ~20 km asl) and the comparison yielded that the Rayleigh clear HLOS wind speed presented an approximately equal overestimation and underestimation, while the Mie cloudy HLOS wind speed was significantly overestimated. Spin-off analyses were performed in order to test how the spatiotemporal collocation of the radiosonde affected the results.

1 Introduction

An overall insight on atmospheric dynamics is fundamental to aerosol and cloud studies, as well as for their source region and the areas overpassed (Stocker et al., 2013). Additionally, aerosol and cloud radiative effects still present exceptionally large uncertainties nowadays (Myhre et al., 2013). However, there is a current lack of accurate worldwide near-real-time



atmospheric dynamics tracking in the Global Observing Systems (GOS), which affects the reliability of Numerical Weather Prediction (NWP) models (WMO, 2004). For this aim, the European Space Agency (ESA) developed a satellite mission able to provide worldwide vertically-resolved wind information, especially in poorly monitored regions such as the tropics, the poles and the oceans (Andersson, 2018; Stoffelen et al., 2020; Straume et al., 2020).

35 Aeolus was launched in August of 2018. The satellite, with a single meteorological instrument, the Atmospheric LAsEr Doppler INstrument (ALADIN), was put into a Sun-synchronous orbit around the Earth. ALADIN is the first Doppler lidar system into space and the first system to measure non-stop global wind information in the line-of-sight (LOS) of the satellite's laser beam. ALADIN consists of a set of two interferometers, which allow the instrument to detect the Doppler shift caused by molecules (Rayleigh channel) and particles (Mie channel) in the backscattered signal (ESA, 2008; Ingmann and Straume, 2016; Rennie et al., 2020; Stoffelen et al., 2020). Since the satellite launch, Aeolus processing chain changed and product versioning has been updated, with subsequent improvements and fixings in order to provide valuable near-real-time information that can be assimilated by the NWP models. Aeolus provides different product levels, namely L1B preliminary wind data, L2B fully processed wind data and L2C wind fields after being processed under NWP models. Additionally, Aeolus provides L2A optical information about the atmospheric components along with geolocation information and metadata.

Aeolus performance and product quality have been widely studied. Prior to the satellite's launch, a wide set of calibration and validation (Cal/Val) activities were planned by ESA. Cal/Val activities have focused on Aeolus L2B wind products, which have been validated with NWP models (Chen et al., 2021; Martin et al., 2021), ground-based (Khaykin et al., 2020; Belova et al., 2021; Guo et al., 2021; Iwai et al., 2021; Ratynski et al., 2022; Wu et al., 2022) and other suborbital instrumentation (Baars et al., 2020; Lux et al., 2020, 2022a; Witschas et al., 2020, 2022; Bedka et al., 2021; Chen et al., 2021; Iwai et al., 2021; Martin et al., 2021). Parallely, some Cal/Val activities have assessed Aeolus L2A optical products with ground-based (Baars et al., 2021; Abril-Gago et al., 2022; Gkikas et al., 2022) and other space-borne instrumentation (Feofilov et al., 2021). Thanks to these Cal/Val activities, Aeolus wind products have reached enough scientific quality and have already been assimilated by NWP models with positive impact, improving their reliability (Rennie et al., 2021; Rennie and Isaksen, 2020), achieving an important mission objective within its nominal life of three years (von Bismarck, 2022). Aeolus nominal life was set to end at November 2021, although it has been extended to December 2022, depending on fuel availability (von Bismarck, 2022).

This work presents the Cal/Val activities of Aeolus wind products developed at Granada, a facility belonging to the Aerosol Clouds and Trace gases Research InfraStructure (ACTRIS) and the Andalusian Global ObseRvatory of the Atmosphere (AGORA), with collocated Doppler lidar system and radiosonde station. The article is structured as follows: Section 2 is devoted to the comparison experimental setup, the satellite and the instrumentation used in the ground-based station; Section 3 explains the methodology, criteria considered in the activities and quality control applied to the different datasets; Section 4 presents the results and discussion of the comparison activities; and Section 5 states the main findings of the Cal/Val activities and Aeolus wind products performance.



65 2 Instrumentation and experimental site

2.1 The Aeolus satellite

Aeolus was put in a Sun-synchronous orbit at 320 km around the Earth on the 22nd August 2018. Completing an orbit in around 90 min, it provides a full coverage of the Earth every week (revisit time of 7 days). The main Aeolus's payload is ALADIN, an instrument based on the Doppler lidar technique which allows the retrieval of wind velocity information based on the Doppler shift of the backscattered radiation. The instrument consists of a Nd:YAG laser transmitter generating 355 nm pulses and a dual channel receiver, that is a Fabry-Pérot interferometer registering the Doppler shift caused by molecules known as Rayleigh channel, and a Fizeau interferometer registering the Doppler shift caused by particles (clouds and aerosols) known as Mie channel (ESA, 2008; Reitebuch, 2012). In clear conditions, the Rayleigh channel provides the majority of the wind data, while the Mie channel provides significant wind data under scenarios of optically thin clouds and thick aerosol layers (Martin et al., 2021).

Aeolus provides the horizontal projection of the wind velocity information in the LOS of the laser beam, i.e., the horizontal component of the LOS (HLOS wind speed), which is a variable able to sufficiently characterize wind fields (ESA, 2008). Wind speed is measured in vertical profiles from surface up to around 30 km, divided into 24 vertical bins with a variable vertical resolution of, nominally, 0.5 km between 0 and 2 km, 1 km between 2 and 16 km and 2 km between 16 and 30 km (ESA, 2008; Ingmann and Straume, 2016). To achieve enough signal-to-noise ratio (SNR), each wind measurement corresponds to an accumulation of 20 laser pulses, ~2.9 km horizontally, and 30 measurements are averaged into a single observation, of around 87 km, that sets the Aeolus' horizontal resolution. Due to the larger backscatter caused by particles (i.e., larger SNR), the Mie channel horizontal resolution was increased to 10 km (Šavli et al., 2019).

Aeolus processing chain retrieves the wind information from the signals. Aeolus wind products are labelled Level2B (preliminary level 1 products are also available), containing HLOS wind speed information for the Mie and Rayleigh channels (Rennie et al., 2020). L2B products are processed under the European Centre for Medium-range Weather Forecasts (ECMWF) model and the improved wind fields (wind vectors) are classified as L2C products. Additionally, the Doppler lidar technique is able to retrieve optical information (particle backscatter and extinction coefficients) of the atmospheric components from the backscattered signal, classified as L2A products (Flamant et al., 2020; Flament et al., 2021). Aeolus products are available at Aeolus online dissemination: <https://aeolus-ds.eo.esa.int> (last access: 17 October 2022).

The processing chain also provides quality flags and error estimates of the wind data and includes a scene classification (Rennie et al., 2020). For each bin, quality flags address different parameters related to the measured signal, from ground echo interference to SNR thresholds. Error estimates provide an estimation of the accumulated error of each bin. Finally, the processing chain applies a scene classification based on the backscatter ratio (total-to-molecular backscatter coefficient ratio) to determine if each bin information corresponds to a cloud or a clear atmospheric region (Tan et al., 2017; Reitebuch et al., 2018). Aeolus is able to provide up to four separate wind configurations, namely Mie cloudy, Mie clear, Rayleigh cloudy



and Rayleigh clear. However, only the Mie cloudy and the Rayleigh clear configurations are generally used (Lux et al., 2020; Martin et al., 2021).

100 From previous Cal/Val activities, critical malfunctioning was identified and processing improvements were achieved. Aeolus processing chain updates were released in the form of baseline versions. Two main error sources were identified. Wind biases caused by variations of the primary telescope mirror temperature were detected and reduced, and fluctuations of the dark current signals on the detectors were characterized (Rennie and Isaksen, 2020; Weiler et al., 2021a, 2021b). With these updates, Aeolus wind products were included into NWP models and weather services, allowing the satellite to prove its positive impact on the accuracy of model forecasts, especially over the tropics and the poles (Rennie et al., 2021; Rennie and
105 Isaksen, 2020). From the beginning of the Aeolus mission, several baselines were released, especially in the first year of the mission. Baseline 10 (B10, released in October 2020) entailed a reprocessing of a large dataset of Aeolus products (from July 2019 to December 2019 and from April 2020 to October 2020) under a homogeneous processing including the fixing of the detected problems and errors. The Cal/Val community is encouraged to use versioning B10 and ahead.

The satellite is constantly checked and laser sensitivity tests (and other analysis) are frequently being performed. This,
110 together with malfunction periods, causes the instrument regular operation to be rarely interrupted (e.g., March 2021 due to instrument anomalies). For these reasons, validity flags have to be taken into account. Additionally, Aeolus regular operation has undergone other major changes. During the second half of June 2021 Aeolus orbit setting changed from ANX4.5 to ANX2.0 in the framework of upcoming tropical campaigns activities in Cape Verde (Fehr et al., 2021, 2022; Lux et al., 2022b): Joint Aeolus Tropical Atlantic Campaign (JATAC), causing the orbit characteristics (e.g., ground track) to
115 significantly shift.

2.2 Granada ACTRIS/AGORA facility

AGORA (Andalusian Global Observatory of the Atmosphere) is an observational platform in the frame of ACTRIS in Andalusia (Spain). The ACTRIS/AGORA station in Granada (37.164° N, 3.605° W; 680 m a.s.l.) is located in a rather populated region with significant presence of anthropogenic particles throughout the year (Lyamani et al., 2010; Casquero-
120 Vera et al., 2021). The station is placed in a hot spot between Europe and Africa with frequent mineral dust intrusions coming from the Sahara Desert (e.g., Guerrero-Rascado et al., 2008, 2009; Navas-Guzmán et al., 2013; Bravo-Aranda et al., 2015; Granados-Muñoz et al., 2016) and notable concentrations of continental aerosols coming from the European continent (Lyamani et al., 2010). The presence of fresh and aged wildfire smoke is also common (Alados-Arboledas et al., 2011; Ortiz-Amezcuca et al., 2014, 2017; Sicard et al., 2019), while significant concentrations of bioaerosol particles (pollen grains) of
125 some anemophilous species are yearly detected during the main pollen season (Cariñanos et al., 2021). In the last years, the region has suffered extreme episodes of particulate matter, for both mineral dust (Cazorla et al., 2017; Fernández et al., 2019; López-Cayuela et al., 2021) and pollen grains (Cariñanos et al., 2022). The city is located in a natural basin at the foot of Sierra Nevada, with altitude up to 3000 m a.s.l., affecting the diurnal (thermal flow between the mountain and the basin) and night (katabatic winds from the mountain) wind regimes (Montálvez et al., 2000; Ortiz-Amezcuca et al., 2022a). Historical



130 records yield mean winds of less than 2 m/s at surface level generally coming from west and northwest (Bosque-Maurel, 1959; Viedma-Muñoz, 1998). A more detailed and recent description of wind patterns at the city of Granada is given by Ortiz-Amezcuca et al. (2022a).

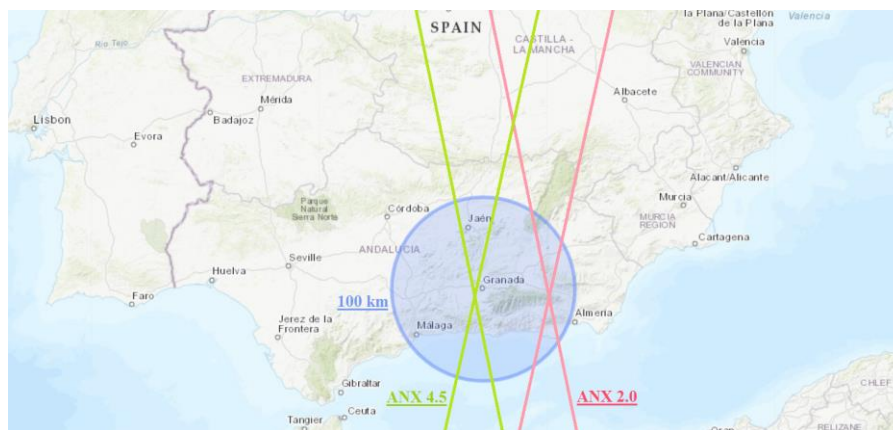
A wide variety of in-situ and remote sensing instrumentation is routinely operated at the ACTRIS/AGORA station in Granada. In particular, a Halo Photonics StreamLine Doppler lidar system has worked continuously since April of 2016. 135 Similarly to ALADIN, this system is able to detect the Doppler shift caused by the atmospheric components in the backscattered signal. However, due to the different signal strength of the Halo Photonics StreamLine Doppler lidar, the exploitable signal is limited to the one backscattered by particles (e.g., aerosol particles and clouds). The instrument, integrated into ACTRIS/Cloudnet (Illingworth et al., 2007), emits 1500 nm radiation at 15 kHz and with a heterodyne detector (Pentikäinen et al., 2020) is able to retrieve wind profiles with a vertical resolution of 30 m, tunable temporal 140 resolution down to 2 s, and full-overlap height of around 60 m agl. The horizontal wind components are obtained through the velocity-azimuth display approach (Browning and Wexler, 1968), a method through which the Doppler lidar system scans the atmosphere forming a cone with the laser beam, in this case, every 10 min with an elevation of 75°. A detailed description of the instrument is given by Pearson et al. (2009), while Ortiz-Amezcuca et al. (2022a) gives more details about this particular instrument and the processing of the signals to provide different wind and turbulence products. A wide range 145 of topics can be addressed with Doppler lidar measurements, from atmospheric boundary layer (ABL) characterization (e.g., de Arruda Moreira et al., 2018) to wind patterns characterization (e.g., Ortiz-Amezcuca et al., 2022a, 2022b), generally limited to the lower troposphere.

In addition to Doppler lidar measurements, lightweight weather radiosondes DFM-09 (GRAW) are occasionally launched at the station. These radiosondes provide vertically-resolved measurements of horizontal wind speed and direction, relative 150 humidity, pressure and temperature with high accuracy and resolution using in-situ measurements. The vertical resolution depends on the ascending speed, which is around 10 m for a vertical speed of around 5 m/s. In particular, for the sensors used in these radiosondes the wind speed measurements present a resolution and accuracy of 0.1 and 0.2 m/s, respectively. However, for many purposes the use of radiosondes is constrained because of the low frequency of launches, the equipment costs and the horizontal drift they may suffer (Vaughan et al., 1988). Despite these inconveniences, radiosondes are widely 155 used for ABL characterization (e.g., de Arruda Moreira et al., 2018; Granados-Muñoz et al., 2012), aerosol hygroscopic growth (e.g., Bedoya-Velásquez et al., 2018) and instrument validation (e.g., Navas-Guzmán et al., 2014; Bedoya-Velásquez et al., 2019), among others.

The location of AGORA and the available uplooking instrumentation allows the station to contribute to the validation activities of Aeolus wind products with ground-based Doppler lidar systems and radiosondes. The satellite overpasses the 160 station twice per week every Thursday. Prior to the orbit shift (ANX4.5) the overpasses took place at approximately 06:24 (descending orbit) and 18:04 UTC (ascending orbit) at around 24 km west (nominal predicted minimum distance between the satellite and the station). After the orbit shift (ANX2.0) the overpass times slightly changed to 06:17 and 17:57 UTC while the overpass distances significantly increased to around 70 km east, on the opposite side of Sierra Nevada. The two



orbit settings fulfil ESA's requirements, i.e., Aeolus products within 100 km of a station should be considered into a
165 comparison activity (Straume et al., 2019). Figure 1 illustrates the Aeolus overpasses under the ANX2.0 and ANX4.5 orbits
considered in this work.



170 **Figure 1: Aeolus orbit settings considered in the work. Green lines indicate ANX4.5 orbits prior to the June-2021 orbit shift and pink lines indicate ANX2.0 orbits after the June-2021 orbit shift. The Sierra Nevada mountainous system can be observed to the east of Granada. © OpenStreetMap contributors 2022. Distributed under the Open Data Commons Open Database License (ODbL) v1.0.**

3 Methodology

3.1 Data

175 Aeolus can provide up to four independent wind estimations. In this work, only the Rayleigh clear and Mie cloudy configurations were considered. The Rayleigh clear configuration provided most of the wind estimates, which extended from surface up to 18 km asl, approximately, while the Mie cloudy configuration was limited to estimates within clouds (or high backscatter conditions), where the configuration could provide several wind estimates even for the same bin height, presenting a vertical coverage limited to the cloud extension (generally between the surface and 12 km asl). Radiosonde vertical coverage depends on the balloon type and can change for each independent launch. In our case, all the balloons were
180 able to fully cover the troposphere and the lower stratosphere (~20 km asl). The ground-based Doppler lidar system is highly dependent on the ABL conditions, and it rarely provides wind information above 3 km asl, except under the presence of advected aerosol layers or cloud conditions. The comparison in this study was performed using the largest possible vertical range in each case.

185 Aeolus quality and validity flags were considered and only valid bins were used for comparison purposes. Aeolus error estimates were also considered and an initial filtering of Aeolus bins was performed. Thus, Rayleigh and Mie bins with error estimates larger than 8 and 4 m/s, respectively, were filtered out of the comparison (Witschas et al., 2020; Wu et al., 2022).



190 Previous studies applied this kind of filtering with similar thresholds for the Rayleigh and Mie channels, such as 7 and 5 m/s (Guo et al., 2021), 8 and 5 m/s (Belova et al., 2021; Iwai et al., 2021) and 6 and 4 m/s (Martin et al., 2021), respectively. Following Witschas et al. (2020), around 94.5 % of Rayleigh and 97 % of Mie bins were available for the comparison in this work. Furthermore, only Aeolus L2B products under B10 baseline and later versioning were considered in this study, following the Cal/Val community recommendations.

3.2 Comparison setting

In the case of the comparison between Aeolus and the ground-based Doppler lidar system, the temporal coverage started on July 2019 with B10 and ended on the second half of June 2021 (the period from January to June 2020 was not reprocessed under B10), with the planned orbit shift. 144 overpasses were available for this period. However, 109 overpasses were coincident in space and time with ground-based Doppler lidar measurements. Additionally, a short comparison was made between Aeolus and ground-based Doppler lidar measurements after the orbit shift, with 85 overpasses (B12), in order to test if the comparison worsens or not. The decision to stop the comparison after the orbit shift was based mainly on the facts that (i) the orbit setting changed significantly, (ii) the average overpass minimum distance increased from around 24 km to 70 km and (iii) Aeolus overpasses would now take place at the opposite side of Sierra Nevada, with significantly different topography and wind regimes especially in the lower troposphere (the region that mainly measures the ground-based Doppler lidar system). Finally, a 30-min interval around the overpass time was taken to average ground-based Doppler lidar measurements into a single profile (Wu et al., 2022). Other studies used a one-hour interval (e.g., Belova et al., 2021; Iwai et al., 2021) or a two-hour interval (e.g., Khaykin et al., 2020), and these criteria were also tested in spin-off comparisons.

205 A special campaign between Aeolus and the radiosondes was planned after the orbit shift and only B12 Aeolus products could be used. Seven radiosondes were launched spatiotemporally matching Aeolus overpasses between June 2021 and July 2022. In the case of the radiosondes, it took some time for the sensor to rise. In order to obtain a fairly acceptable spatial and temporal coincidence, the radiosondes were launched around 30 min before Aeolus overpassed the station, so that the radiosonde were at around 9 km (generally around half altitude of radiosounding's vertical coverage) at that moment. This setting sought to maximize the spatiotemporal collocation of the measurements, which allowed us to properly detect the satellite bias unlike previous Cal/Val campaigns in which radiosondes were launched well in advance or late (e.g., Chen et al., 2021). In order to test this criterion, 5 different radiosondes (not fulfilling the 30-min in advance launch) were considered in a spin-off comparison with Aeolus products. Additionally, radiosonde's horizontal drift was also taken into account in order to consider if measurements were spatially collocated for each bin.

215 Furthermore, a distinction between ascending and descending overpasses was considered for the comparison between Aeolus and each uplooking instrument.



3.3 Preparatory processing

The comparison was performed with Aeolus HLOS wind speed measurements, $V_{HLOS_{Aeolus}}$, which is the horizontal speed component in the line-of-sight of Aeolus' laser beam. Additionally, Aeolus provided the azimuth angle, φ_{Aeolus} , which is the horizontal projection of the laser beam pointing vector measured clockwise from north and takes approximate values of 100° or 260° for descending or ascending orbits. Both variable profiles presented the same variable vertical resolution mentioned in Section 2.1. On the other hand, the uplooking instrumentation measured the horizontal wind velocity and its direction (i.e., zonal, u , and meridional, v , wind components). Thus, the HLOS wind was extracted from ground-based Doppler lidar and radiosonde measurements as:

$$V_{HLOS_{UL}} = -u_{UL} \cdot \sin \varphi_{Aeolus} - v_{UL} \cdot \cos \varphi_{Aeolus} \quad (1)$$

where $V_{HLOS_{UL}}$, u_{UL} and v_{UL} are the HLOS, zonal and meridional components derived by the uplooking instruments, respectively, and φ_{Aeolus} is Aeolus azimuth angle. Equivalently, the following expression could be used:

$$V_{HLOS_{UL}} = V_{UL} \cdot \cos (\varphi_{Aeolus} - \varphi_{UL}) \quad (2)$$

where V_{UL} and φ_{UL} are the total horizontal speed and direction derived by the uplooking instruments, respectively. In order to extract this component, the vertical resolution of the uplooking instrument profiles had to be degraded in order to match the much coarse vertical resolution of the Aeolus profiles.

3.4 Statistical analysis

Two independent bin-to-bin comparisons were performed between Aeolus HLOS winds and each uplooking instrument's HLOS winds. For each of these comparisons, the differences between each Aeolus channel and the uplooking instruments were calculated as:

$$\Delta = V_{HLOS_{Aeolus}} - V_{HLOS_{UL}} \quad (3)$$

Thus, $\Delta > 0$ ($\Delta < 0$) yielded an overestimation (underestimation) of HLOS wind speed by Aeolus. In order to get the vertical distribution of this parameter, the mean Δ between Aeolus and the uplooking instruments was calculated in 0.5 and 2 km vertical intervals for the ground-based Doppler lidar and radiosondes, respectively. Thus, the mean Δ between Aeolus and the instruments was calculated as:

$$\Delta(r) = \frac{1}{N} \sum (V_{HLOS_{Aeolus}}(z) - V_{HLOS_{UL}}(z)) \quad (4)$$

where r is the vertical interval of 0.5 or 2 km, z is the bin's mean altitude (z lies within r) and N is the number of bins whose z lies within r . Additionally, the root-mean square error was calculated as:

$$RMSE(r) = \sqrt{\frac{1}{N} \sum (V_{HLOS_{Aeolus}}(z) - V_{HLOS_{UL}}(z) - \Delta(r))^2} \quad (5)$$

On the other hand, a linear fitting of $V_{HLOS_{UL}}$ against $V_{HLOS_{Aeolus}}$ was performed, and the slope, intercept and Pearson linear correlation coefficient, R , were obtained.



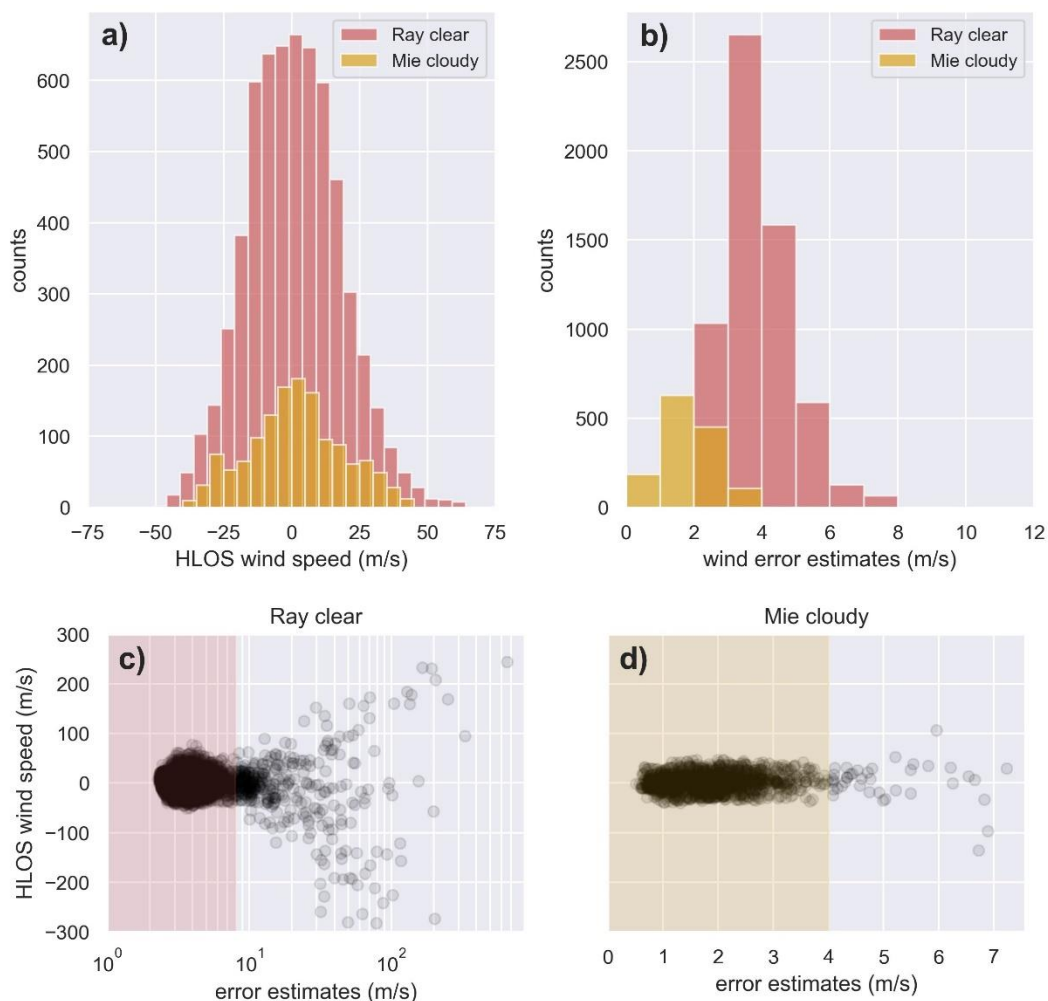
4 Results and discussion

First, a general analysis of the Aeolus performance was developed with all the available overpasses from July 2019 until the orbit shift of June 2021. Then, two independent comparisons were performed: one between Aeolus and the ground-based Doppler lidar system and another one between Aeolus and the radiosondes. Spin-off analyses were performed in order to verify that the chosen criteria for the comparison were valid.

4.1 Evaluation of Aeolus' general performance

144 overpasses were available for the evaluation of Aeolus' general performance, from July 2019 until June 2021 orbit shift. 101 were B10 while 43 were B11, from which half of them corresponded to ascending orbits and the other half to descending orbits. B12 versioning was released with the orbit shift of June 2021 and no B12 overpasses were considered in this subsection. Considering Aeolus products with ground track within a 100 km distance to the station, 6410 (1416) Rayleigh clear (Mie cloudy) bins were available. From these, 5.6 % (2.8 %) of the available Rayleigh clear (Mie cloudy) bins exceeded the error threshold of 8 m/s (4 m/s) aforementioned in Section 3.1, accounting to 358 (40) filtered out bins. The mean minimum distance (\pm standard deviation, SD) between the Aeolus ground track to the station for the Rayleigh clear (Mie cloudy) bins was 19 ± 10 (14 ± 9) km, while the mean distance (\pm SD) between Aeolus bins to the station was 54 ± 17 (51 ± 27) km.

The mean HLOS wind speed value (\pm SD) was 1 ± 17 (2 ± 17) m/s for the Rayleigh clear (Mie cloudy) configuration, while the mean HLOS wind speed error estimate (\pm SD) was 4 ± 1 (1.8 ± 0.7) m/s. If no filtering had been applied to the error estimates, the mean HLOS wind speed and mean HLOS wind speed error estimate would have been 2 ± 18 (0 ± 25) m/s and 5 ± 13 (1.9 ± 0.9) m/s, respectively, for the Rayleigh clear (Mie cloudy) configuration. Figures 2a and 2b present the histogram of the HLOS wind speeds and its error estimates for the Rayleigh clear and Mie cloudy configurations. Figures 2c and 2d present the HLOS wind speed error estimates versus HLOS wind speeds for the whole database without filtering the error estimates values. It can be seen that the Rayleigh clear configuration presented bins with large and unrealistic HLOS wind speed values (maximum value of around 244 m/s) and equivalently unrealistic error estimates (maximum value of around 655 m/s). In the case of the Mie cloudy configuration, some bins presented unrealistic HLOS wind speed values (maximum value of around 106 m/s) but not unrealistic error estimates (maximum value of around 7 m/s). After applying the filtering, the maximum HLOS wind speed detected with the Rayleigh clear (Mie cloudy) configuration was around 77 (47) m/s, which might correspond to outlier but feasible winds. Thus, the application of the chosen criteria (Witschas et al., 2020) is plausible in order to filter out unrealistic and invalid wind estimations. Moreover, it is worth mentioning that the number of filtered out bins increased when the altitude decreased, as the signal-to-noise ratio decreased.



280 **Figure 2: Histograms of the 144 overpasses (considering the error estimates filtering) for Aeolus estimations for: (a) HLOS wind speed and (b) HLOS wind error estimates. Scatter plot of error estimates versus HLOS wind speeds for the 144 overpasses without considering the error estimates filtering for: (c) Rayleigh clear and (d) Mie cloudy. The red (yellow) area indicates the Rayleigh clear (Mie cloudy) bins valid according to the error estimate filtering (Witschas et al., 2020). Note the different scales in the x-axis.**

Additionally, the unused configurations Mie clear and Rayleigh cloudy provided 7 and 2350 bins, respectively. This number of points was reduced to 0 and 270 bins, respectively, after considering the error estimates filtering, so the 100 % and the 86 % of these bins were filtered out, corroborating that these configurations are not useful for Cal/Val activities (Lux et al., 2020).



285 4.2 Aeolus and the ground-based Doppler lidar comparison

The main statistical results of this section are gathered in Table 1. From the 109 Aeolus overpasses coincident with Doppler lidar measurements, half corresponded to ascending modes of Aeolus overpasses and half to descending overpasses. A total of 4585 (1169) Rayleigh clear (Mie cloudy) bins were available. For both configurations half of the bins corresponded to descending overpasses (~06:24 UTC) and the other half to ascending overpasses (~18:04 UTC), so both datasets were
290 equally significant. The mean minimum distances between the Aeolus ground track to the station were the same as the ones obtained at the general performance analysis, as well as the mean distances between Aeolus bins and the station. However, only 104 (163) Rayleigh clear (Mie cloudy) bins were coincident with ground-based Doppler lidar measurements, a 2.3 % (14 %) of the initially available bins. From these Rayleigh clear (Mie cloudy) bins, the 40 % (48 %) corresponded to descending overpasses. In the case of the Rayleigh clear configuration, the fewer number of coincident bins during
295 descending overpasses was generally associated to the ABL dynamics, typically less developed early morning (~06:24 UTC) than in late evening (~18:04 UTC), restricting the vertical coverage of the ground-based Doppler lidar measurements with enough SNR. It is important to note, as it will be discussed later, that these results and the following ones are valid only for altitudes lower than 3.0 km asl, as most of the available bins fell below this altitude.

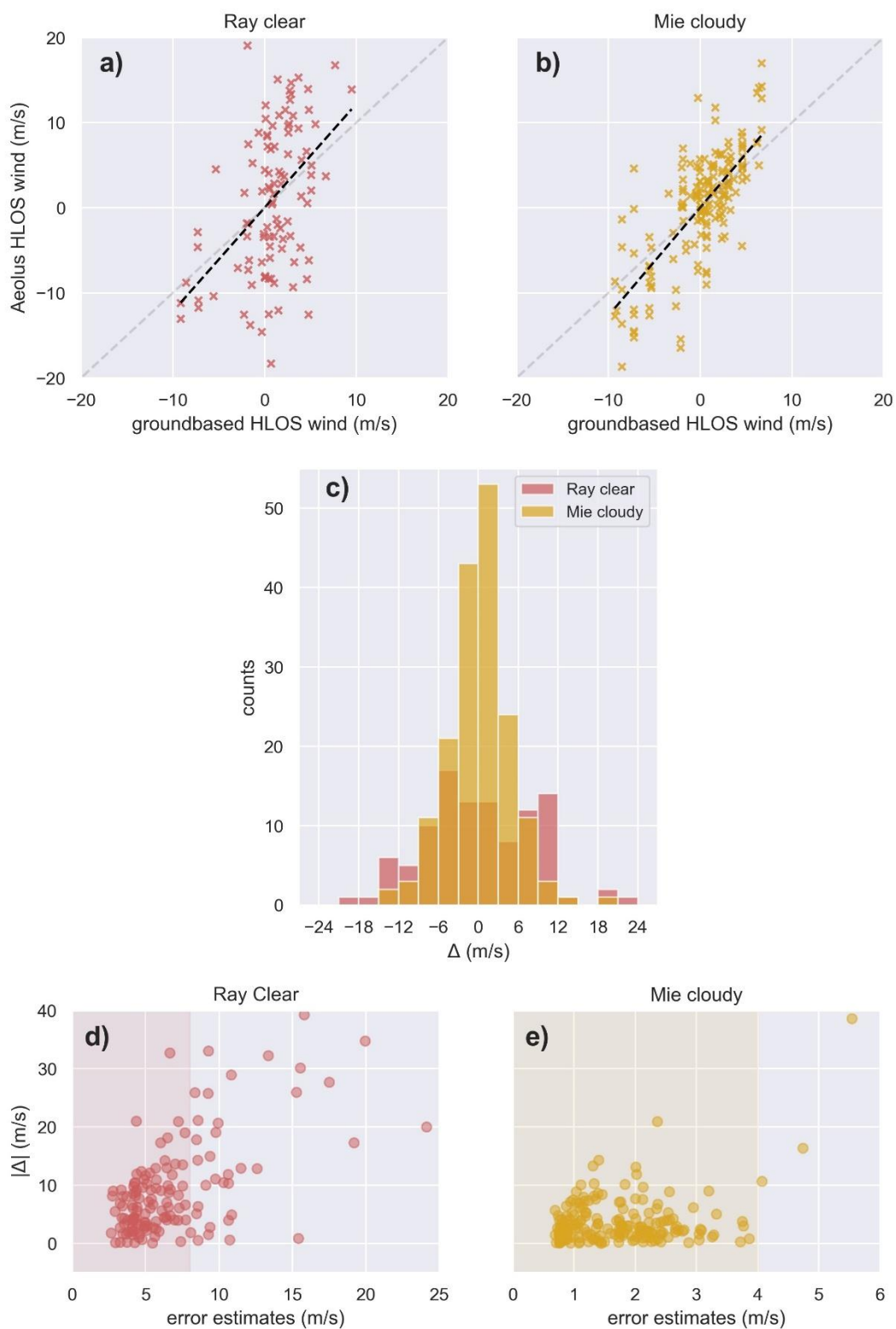
A linear fitting was performed for the pairs of values. Results from the linear fittings are presented in Figures 3a and 3b. The
300 slope, intercept (\pm standard error, SE) and Pearson correlation coefficient were 1.2 ± 0.2 (1.3 ± 0.1), 0.4 ± 0.9 (0.3 ± 0.4) m/s and 0.43 (0.72), respectively, for the Rayleigh clear (Mie cloudy) bins. The slopes were similar for both configurations, while the intercept was slightly higher (in absolute values) for the Rayleigh clear configuration. However, the statistical significance was significantly higher for the Mie cloudy configuration, along with lower coefficient uncertainties than for the Rayleigh clear configuration. The obtained slopes are significantly larger than those reported by Iwai et al. (2021) and Wu et al. (2022) of 0.98 (1.02) and 0.96 (0.92), respectively for the Rayleigh clear (Mie cloudy) configuration, for ground-based
305 Doppler lidars and B10 and B11 products separated less than 100 km, while their obtained intercepts are slightly higher, i.e., -0.88 (0.22) m/s and -1.2 (-0.33) m/s, respectively.

Figure 3c presents the distribution of the bins' differences between Aeolus and the ground-based Doppler lidar system. The mean difference (\pm SD) of the distribution (which can be taken as Aeolus HLOS wind speed bias) was 0 ± 9 (-1 ± 7) m/s for
310 the Rayleigh clear (Mie cloudy) configuration, which yields that Aeolus overestimated ($\Delta > 0$) and underestimated ($\Delta < 0$) approximately equally the HLOS wind speed. These values agree with the 0 m/s global bias reported by von Bismarck (2022) and also with the results reported by Iwai et al. (2021) and Wu et al. (2022), that is -0.81 (-0.16) m/s and -1.15 (-0.25) m/s, respectively, for the Rayleigh clear (Mie cloudy configuration). On the other hand, the mean value (\pm SD) of the absolute difference ($|\Delta|$) was 7 ± 5 (5 ± 5) m/s for the Rayleigh clear (Mie cloudy) configuration, which yields the mean
315 disagreement between Aeolus and the ground-based Doppler lidar.

Figures 3d and 3e show Aeolus error estimates versus the obtained absolute difference between Aeolus and ground-based Doppler lidar measurements. In the case of the Rayleigh clear configuration, significant absolute differences were more



320 frequent for larger error estimates, but a statistically significant relation could not be found for this configuration or the Mie cloudy configuration (nor for the numerical difference). Additionally, it could be confirmed that the error estimates thresholds were efficient for the filtering of large absolute differences (associated to SNR issues and not to instrumental biases), especially for the Rayleigh clear configuration. The threshold could be increased to 5 m/s for the Mie cloudy bins, but only 2 new bins could be available, with similar statistical results.





325 **Figure 3: Pairs of Aeolus and ground-based Doppler lidar system values for the: (a) Rayleigh clear and (b) Mie cloudy configurations. The linear fitting is marked by the black dashed line, while the light gray dashed line marks the 1:1 relation. (c) Histogram of the differences between Aeolus and the ground-based Doppler lidar measurement. Scatter plot of Aeolus error estimates versus absolute difference between Aeolus and ground-based Doppler lidar measurements for the: (d) Rayleigh clear and (e) Mie cloudy configurations. The red (yellow) area indicates the Rayleigh clear (Mie cloudy) bins valid according to the error estimate filtering (Witschas et al., 2020).**

330

An analysis of the differences and RMSE per 0.5 km vertical steps is presented in Figure 4. Most of the available bins were constrained between approximately the station's altitude (~0.68 km asl) and 3.0 km asl. The Rayleigh clear configuration (Figure 4a) did not present any specific behavior between 0.5 and 3.0 km asl (values between -1 and 0.3 m/s), except between 1.5 and 2.0 km asl where the satellite significantly overestimated the HLOS wind speed (~3 m/s). The RMSE (Figure 4b) was significantly large for the lowermost bins (~12 m/s), while the rest of vertical intervals presented a similar lower value (between 7 and 8 m/s), except the interval between 2.5 and 3.0 km asl where the RMSE was lower (~5 m/s), along with the statistical significance. The Mie cloudy configuration (Figure 4c) seems to significantly overestimate the HLOS wind speed for the lowermost bins (~4 m/s), while it did not present any specific performance (values between -1.6 and 0.9 m/s) for upper intervals. On the other hand, the RMSE (Figure 4d) presented a higher value for the 2.0 to 2.5 km asl interval and the lowermost interval (~6 m/s) bins, while the middle ranges present a similar lower value (~4 m/s) along with the intervals higher than 2.5 km asl (values between 1.3 and 2 m/s).

335

340

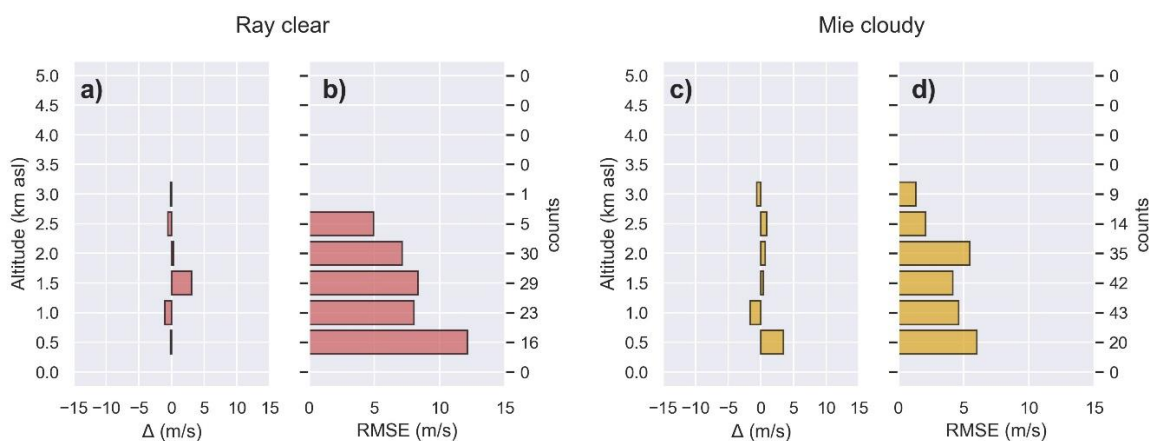


Figure 4: Vertically-resolved analysis of the: (a) difference and (b) RMSE for the comparison between Aeolus Rayleigh clear products and the ground-based Doppler lidar. Panels (c) and (d) are analogous to (a) and (b) for the Mie cloudy products.

345 Table 1 shows the comparison results under different settings, being the first row (Table 1, row a) the main setting (i.e., ANX 4.5 Aeolus ascending plus descending overpasses, with maximum 100 km difference with the ground-based station and 30-min averaging of the ground-based measurements). When differentiating between ascending and descending orbits (Table 1, rows b and c) reasonably different results were obtained for each mode. The ascending mode presented slopes



slightly closer to 1 than the descending mode, along with a significantly lower R coefficient. The slopes were notoriously
350 different between each orbit mode. The mean difference and mean absolute difference were similar for the Rayleigh clear
configuration, while the Mie cloudy configuration presented significantly lower uncertainties for both parameters and the
mean absolute difference itself with the ascending mode dataset.

An analogous analysis was performed taking one-hour (Table 1, row d) and two-hour (Table 1, row e) averages of the
ground-based Doppler lidar measurements. The agreement between the instruments slightly worsened when the average
355 interval increased, especially the slope of the linear fitting. The main analysis was also repeated just decreasing the
maximum distance between the considered bins and the station (fixed 30-min average) to 90, 80, 60 and 50 km (Table 1,
rows f, g, h and i). In this case, it could be seen that when the maximum distance was decreased the slope and intercept
significantly increased (slightly decreased) for the Rayleigh clear (Mie cloudy) configuration. Thus, a more restrictive spatial
colocation of Mie cloudy bins slightly improved the comparison results, as cloud spatial inhomogeneities were avoided.
360 However, the comparison for the Rayleigh clear configuration worsens and for both configurations the number of available
bins is significantly reduced, affecting the statistical significance. A similar examination was performed increasing the
maximum distance between the considered bins and the station to 110 and 120 km (Table 1, rows j and k). It was observed
that when the maximum distance was increased the slope and intercept for the Rayleigh clear slightly reduced but also did
the Pearson correlation coefficient, while the results for the Mie cloudy remained almost unaffected (only the intercept was
365 slightly reduced). Then, it is recommended to work with bins within 100 km to the station, following ESA's requirements.

Another additional analysis was performed with Aeolus overpasses after the orbit shift (Table 1, row l). 85 overpasses
matched with ground-based Doppler lidar measurements from June 2021 to March 2022, half of which correspond to
descending overpasses (~06:17 UTC) and the other half to ascending ones (~17:57 UTC). A total of 2424 (534) Rayleigh
clear (Mie cloudy) bins were available, from which only 46 (87) bins were coincident with ground-based Doppler lidar
370 measurements, a 1.8 % (16 %). The mean minimum distance (\pm SD) between the Aeolus ground track to the station for the
Rayleigh clear (Mie cloudy) bins increased significantly with respect to the previous orbit setting, to 64 ± 15 (61 ± 17) km
for the Rayleigh clear (Mie cloudy) bins, approximately 3 (4) times further. The obtained slope, intercept (\pm SE) and Pearson
correlation coefficient were 0.8 ± 0.4 (0.6 ± 0.1), -1 ± 1 (2 ± 1) m/s, 0.31 (0.42) for the Rayleigh clear (Mie cloudy)
configuration. On the other hand, the mean Δ (\pm SD) was -1 ± 9 (5 ± 11) m/s and the mean $|\Delta|$ (\pm SD) was 8 ± 6 (9 ± 7) m/s,
375 for the Rayleigh clear (Mie cloudy) configuration. The slope of the linear fitting reduced significantly after the orbit shift,
while intercept increased, but most importantly the statistical significance decreased notoriously. The differences between
Aeolus and the ground-based Doppler lidar slightly increased. However, these differences might not be associated with the
new versioning B12 but to the fact that Aeolus overpasses a completely different region. Under orbit ANX2.0 Aeolus
overpasses the opposite side of Sierra Nevada to the one Granada is located, where the altitude and land inclination are
380 significantly different and therefore wind patterns associated with surface insolation change considerably. If this analysis
was repeated taking a two-hour average of the ground-based Doppler lidar measurements the results (Table 1, row m)
worsened considerably.



Table 1: Statistical results of the comparison between Aeolus wind products and ground-based Doppler lidar measurements. For each cell, the upper result refers to the Rayleigh clear configuration, while the lower result refers to the Mie cloudy configuration.

	orbit	ground track max. dist. (km)	ground signal temp. average	bins	mean bins dist. \pm SD (km)	slope \pm SE	intercept \pm SE (m/s)	R	$\Delta \pm$ SD (m/s)	$ \Delta \pm$ SD (m/s)	
(a)	ANX4.5	100	30 min	104	54 \pm 27	1.2 \pm 0.2	0.4 \pm 0.9	0.43	0 \pm 9	7 \pm 5	
(b)	ANX4.5 ascen. mode			163	51 \pm 27	1.3 \pm 0.1	0.3 \pm 0.4	0.72	-1 \pm 7	5 \pm 5	
(c)	ANX4.5 descen. mode			61	57 \pm 26	1.0 \pm 0.4	1.4 \pm 1.3	0.31	1 \pm 9	7 \pm 5	
				79	52 \pm 26	1.1 \pm 0.2	0.7 \pm 0.5	0.61	-1 \pm 3	2 \pm 2	
				43	51 \pm 28	1.2 \pm 0.3	-0.5 \pm 1.3	0.48	1 \pm 8	6 \pm 5	
				84	49 \pm 29	1.3 \pm 0.1	0.1 \pm 0.6	0.71	-1 \pm 10	9 \pm 6	
(d)	ANX4.5	100	1 h	86	54 \pm 27	1.3 \pm 0.3	-0.1 \pm 1.0	0.40	0 \pm 9	7 \pm 5	
(e)			2 h	128	51 \pm 27	1.3 \pm 0.1	-0.2 \pm 0.5	0.70	-1 \pm 9	6 \pm 6	
				80	54 \pm 27	1.5 \pm 0.4	-0.6 \pm 1.1	0.41	0 \pm 9	7 \pm 5	
				119	51 \pm 27	1.4 \pm 0.2	-0.2 \pm 0.5	0.65	0 \pm 10	8 \pm 6	
(f)	ANX4.5	90	30 min	76	49 \pm 25	1.2 \pm 0.3	-0.2 \pm 0.9	0.50	0 \pm 8	7 \pm 5	
(g)		80		158	45 \pm 24	1.2 \pm 0.1	0.3 \pm 0.4	0.71	-1 \pm 7	5 \pm 5	
(h)		60		54	43 \pm 21	1.3 \pm 0.3	-0.5 \pm 1.0	0.56	0 \pm 8	6 \pm 5	
(i)		50		146	41 \pm 21	1.2 \pm 0.1	0.2 \pm 0.4	0.72	-1 \pm 7	5 \pm 5	
(j)		110		31	34 \pm 16	1.5 \pm 0.3	0.7 \pm 1.4	0.64	1 \pm 8	6 \pm 5	
					113	32 \pm 15	1.2 \pm 0.1	0.0 \pm 0.4	0.74	-2 \pm 7	5 \pm 6
					25	28 \pm 12	1.6 \pm 0.4	1.2 \pm 1.5	0.69	2 \pm 7	6 \pm 5
			98	27 \pm 13	1.1 \pm 0.1	-0.1 \pm 0.4	0.71	-2 \pm 8	5 \pm 6		
(k)		120		137	59 \pm 30	1.1 \pm 0.2	-0.1 \pm 0.8	0.38	0 \pm 9	7 \pm 5	
				180	55 \pm 30	1.3 \pm 0.1	0.2 \pm 0.3	0.72	-1 \pm 7	5 \pm 5	
				157	64 \pm 33	1.2 \pm 0.2	0.1 \pm 0.9	0.36	0 \pm 9	8 \pm 6	
				190	60 \pm 33	1.3 \pm 0.1	0.1 \pm 0.3	0.74	-1 \pm 7	5 \pm 5	
(l)	ANX2.0	100	30 min	46	75 \pm 17	0.8 \pm 0.4	-1 \pm 1	0.31	-1 \pm 9	8 \pm 6	
(m)			2 h	87	74 \pm 15	0.6 \pm 0.1	2 \pm 1	0.42	5 \pm 11	9 \pm 7	
				34	75 \pm 17	0.2 \pm 0.6	-3 \pm 1	0.06	-4 \pm 8	7 \pm 6	
				66	74 \pm 15	0.1 \pm 0.3	1 \pm 1	0.06	2 \pm 11	10 \pm 6	



4.3 Aeolus and radiosonde comparison

The main statistical results of this section are gathered in Table 2. Seven radiosondes were launched during Aeolus overpasses under the defined criteria. From these cases, 2 of them correspond to descending modes of Aeolus overpasses and 5 to ascending overpasses. A total of 191 (43) Rayleigh clear (Mie cloudy) bins were available. A 26 % (11 %) of the
390 Rayleigh clear (Mie cloudy) bins correspond to descending overpasses (~06:17 UTC). This distribution inhomogeneity might be associated with the few descending overpasses available, and also to the limited dataset of overpasses itself (29% of overpasses). The mean minimum distance (\pm SD) between the Aeolus ground track to the station for the Rayleigh clear (Mie cloudy) bins was 64 ± 14 (61 ± 16) km, while the mean distance (\pm SD) between the bins and the station was 75 ± 19 (72 ± 17) km. Aeolus bins within 100 km were taken, due to the larger minimum distance between the overpass and the station.

395 From the available dataset, 188 (43) Rayleigh clear (Mie cloudy) bins were coincident with radiosounding measurements, a 98 % (100 %) of the initially available bins. In this case, most of the available bins were coincident with radiosounding measurements thanks to the radiosonde's wide vertical coverage, which generally provides wind information up to the lower stratosphere.

A linear fitting was performed for the pairs of values. Results from the linear fittings are presented in Figures 5a and 5b. The
400 slope, intercept (\pm SE) and Pearson correlation coefficient were 0.96 ± 0.04 (0.84 ± 0.09), 0.3 ± 0.5 (3 ± 1) m/s and 0.87 (0.84), respectively, for the Rayleigh clear (Mie cloudy) bins. The slope for the Rayleigh clear configuration was really close to the 1:1 relation, and the Mie cloudy one was also significantly close. Additionally, for both configurations the statistical significance was fairly acceptable and the uncertainties of their slopes were low. On the other hand, the slopes and statistical significance of these results were much better than the ones obtained with the ground-based Doppler lidar measurements,
405 which were limited to altitudes below 3 km asl, where Aeolus encountered more difficulties to retrieve wind information than for higher altitudes due to the lower SNR. The results obtained for the Rayleigh clear configuration agreed with those reported by Chen et al. (2021) and Iwai et al. (2021) with radiosondes and B10 Aeolus products, that is slopes of 0.97 and 1.01, and intercepts of -0.05 and 0.38 m/s, respectively. The slope obtained for the Rayleigh clear configuration was similar to the one reported by Baars et al. (2020) for previous baseline Aeolus products and radiosondes, while their obtained
410 intercept was significantly larger, that is 0.97 and 1.57 m/s respectively. In the case of the Mie cloudy results, the derived slope was lower and the intercept significantly larger than those obtained by Baars et al. (2020), Chen et al. (2021) and Iwai et al. (2021), that is 0.95, 0.95 and 0.92 and 1.13, -0.01 and -0.22 m/s, respectively.

Figure 5c presents the histogram of the bins' differences between Aeolus and the radiosoundings. The obtained mean difference (\pm SD) was 0 ± 7 (7 ± 10) m/s for the Rayleigh clear (Mie cloudy) configuration. Thus, the Rayleigh clear
415 configuration approximately equally overestimated ($\Delta > 0$) and underestimated ($\Delta < 0$) the HLOS wind speed, while the Mie cloudy configuration seemed to overestimate the HLOS wind speed. The value for the Rayleigh clear configuration agreed with the 0 m/s global bias reported by von Bismarck (2022), and with the one reported by Iwai et al. (2021) for B10 Aeolus

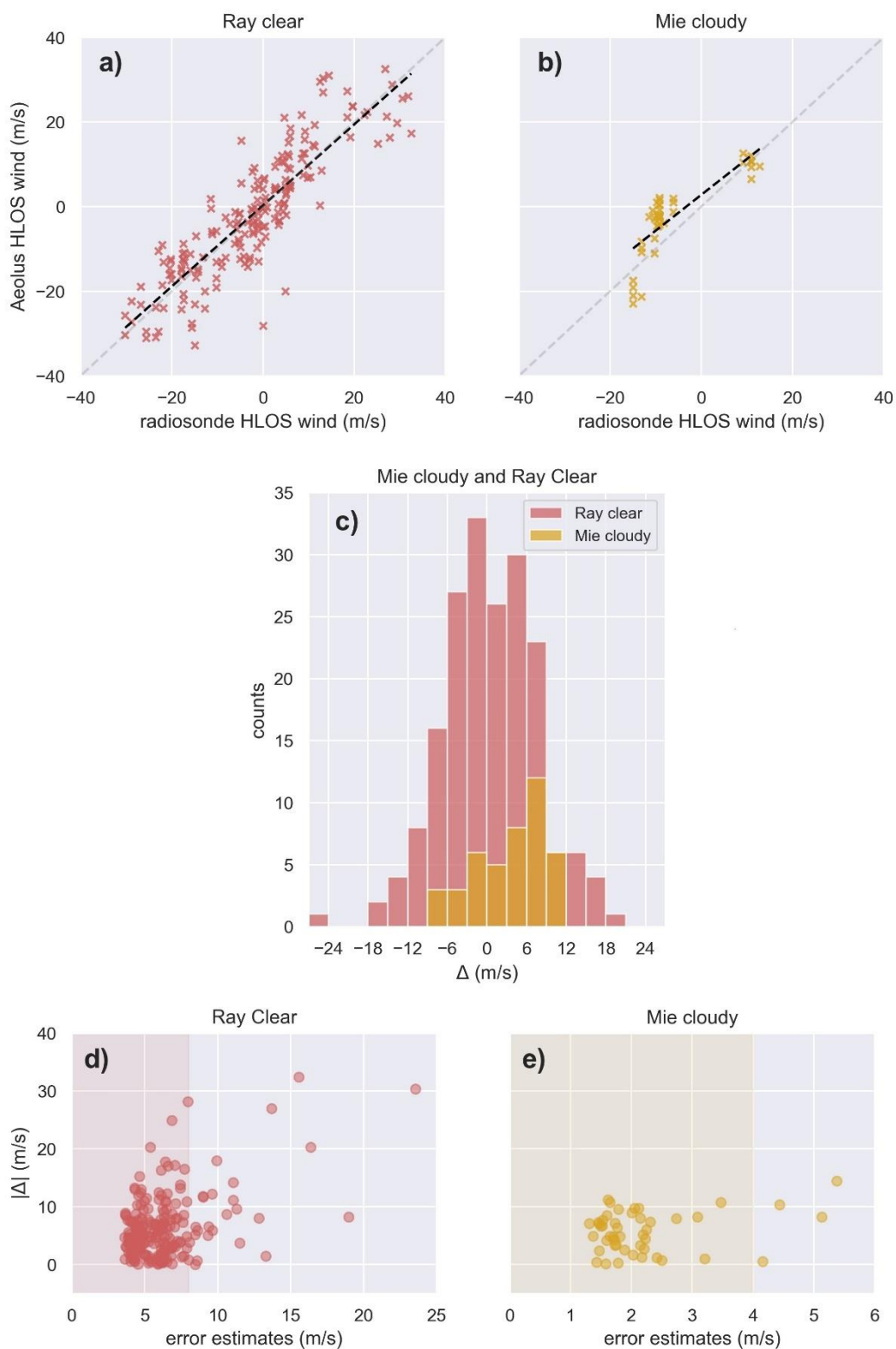


products and radiosondes (0.45), while it was slightly lower than the one reported by Baars et al. (2020), Iwai et al. (2021) and Martin et al. (2021) for previous baseline Aeolus products and radiosondes (1.52, 1.00 and ~2, respectively).

420 On the other hand, the mean value (\pm SD) of the absolute difference ($|\Delta|$) was 6 ± 5 (10 ± 7) m/s for the Rayleigh clear (Mie cloudy) configuration, which yielded the mean disagreement between Aeolus and the radiosondes. In this case, the mean $|\Delta|$ for the Mie cloudy configuration was significantly larger, probably because of the larger distance between Aeolus bins and the radiosondes' measurements. The cloud wind conditions measured by Aeolus might be different to the ones measured by the radiosondes, and even Aeolus might have captured a cloud that the radiosonde have not.

425 Figures 5d and 5e show Aeolus error estimates versus the obtained absolute difference between Aeolus and the radiosondes. In the case of the Rayleigh clear configuration, a couple of significant absolute differences corresponded to larger error estimates, but a significant relation could not be found for this configuration or the Mie cloudy configuration. Additionally, Figures 5d and 5e confirm that the error estimates thresholds were efficient for the filtering of large absolute differences (associated to SNR issues and not to instrumental biases), especially for the Rayleigh clear configuration. A larger threshold

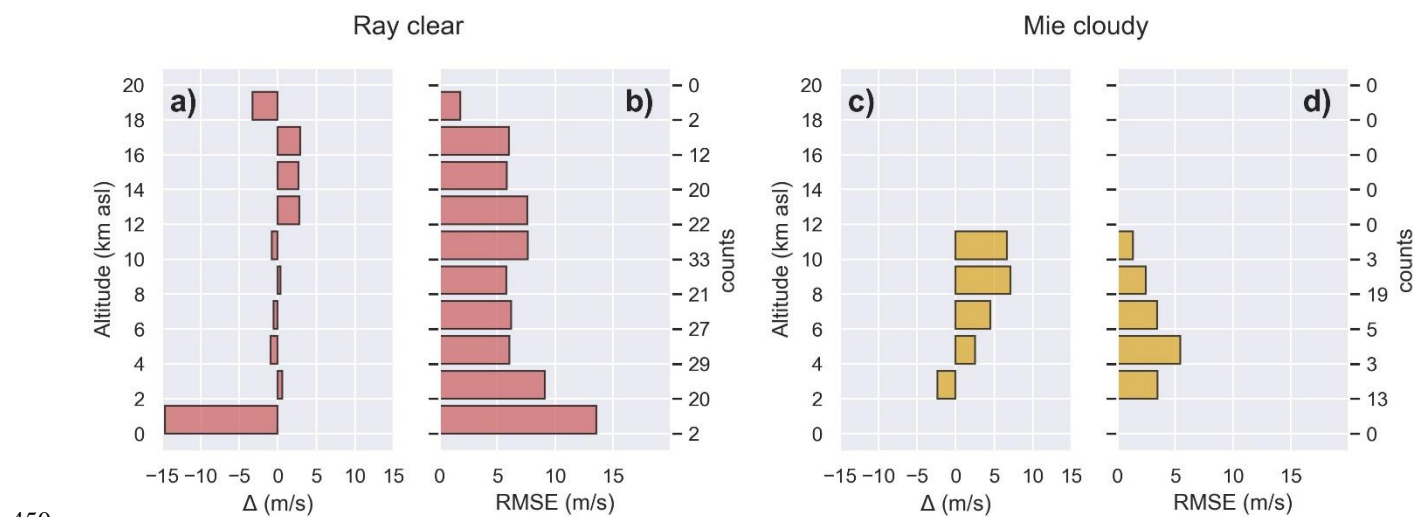
430 could be set in order to consider more bins, for example, 13 (6) m/s for the Rayleigh clear (Mie cloudy) configuration, but the statistical results would not change significantly.





435 **Figure 5: Pairs of Aeolus and radiosonde values for the: (a) Rayleigh clear and (b) Mie cloudy configurations. The linear fitting is marked by the black dashed line, while the light gray dashed line marks the 1:1 relation. (c) Histogram of the differences between**
 440 **Aeolus and radiosonde measurement. Scatter plot of Aeolus error estimates versus absolute difference between Aeolus and radiosonde measurements for the: (d) Rayleigh clear and (e) Mie cloudy configurations. The red (yellow) area indicates the Rayleigh clear (Mie cloudy) bins valid according to the error estimate filtering (Witschas et al., 2020).**

An analysis of the differences and RMSE per 2 km vertical intervals is presented in Figure 6. The Rayleigh clear configuration significantly underestimated the HLOS wind speed between the ground and 2 km asl (Δ of \sim (-15) m/s and
 440 RMSE of \sim 14 m/s). This could be related to the fact that Aeolus overpassed the east side of Sierra Nevada, while radiosondes were launched at the west side, so the lowermost bins (closer to the surface) presented the largest disagreement. However, this interval presented a low statistical significance. Some patterns could be detected for the Rayleigh clear configuration. Aeolus did not present a particular performance between 2 and 12 km asl, with biases close to zero (Δ between -0.9 and 0.6 m/s). Furthermore, the Rayleigh clear configuration significantly overestimated the HLOS wind speed
 445 between 12 and 18 km asl (Δ between 2.7 and 2.9 m/s). The RMSE presented a similar value between 4 and 18 km asl (between 7.6 and 5.7 m/s). On the other hand, the Mie cloudy configuration seemed to significantly overestimate the HLOS wind speed between 4 and 12 km asl (Δ between 2.6 and 7.0 m/s), with the overestimation increasing with altitude. As commented before, the Mie cloudy configuration was highly affected by the clouds itself, so the overestimation seen in Figures 6c and 6d could be associated with cloud scenario inhomogeneities rather than with Aeolus biases.



450 **Figure 6: Vertically-resolved analysis of the: (a) difference and (b) RMSE for the comparison between Aeolus Rayleigh clear products and the radiosondes. Panels (c) and (d) are analogous to (a) and (b) for the Mie cloudy products.**

The results of the analysis differentiating between ascending and descending overpasses are presented in Table 2 (rows b and c). The results obtained for the Rayleigh clear configuration with ascending mode overpasses were similar to those obtained



455 considering both settings together and the statistical significance was slightly reduced, while the Mie cloudy configuration
presented significantly worse agreement with radiosonde measurements with a higher R coefficient. On the other hand, due
to the limited database of cases, only 2 of them correspond to the descending mode and the results obtained for this setting
were significantly worse than those obtained considering both settings together and were not statistically significant,
especially for the Mie cloudy configuration. Thus, the large differences obtained for the descending mode could not be
460 associated with orbit mode biases but most probably with the limited dataset.

An analogous analysis was performed increasing the maximum distance between the considered bins and the station to 110,
120, 140 km (Table 2, rows d, e and f). It could be seen that when the maximum distance was increased the slope slightly
increased while the R coefficient decreased. Thus, a less restrictive spatial collocation slightly worsened the comparison
results. Then, it is recommended to work with bins within 100 km to the station, following ESA's requirements.

465 An additional analysis was performed with both Aeolus overpasses from the same day as each radiosounding, even if the
temporal collocation is not maximized (Table 2, row g). If a radiosonde was launched for the descending overpass, its profile
was also compared with the ascending Aeolus products, and the opposite way. Thus, the maximum time difference was
around 12 h. 12 overpasses matched radiosonde information with these criteria, including the 7 cases previously used and 5
new cases. From the 12 overpasses, half corresponded to descending overpasses and the other half to ascending ones. A total
470 of 332 (69) Rayleigh clear (Mie cloudy) bins were available. The obtained slope, intercept (\pm SE) and Pearson correlation
coefficient were 0.95 ± 0.04 (0.58 ± 0.06), -0.1 ± 0.5 (1.0 ± 0.7) m/s and 0.81 (0.78) for the Rayleigh clear (Mie cloudy)
configuration. On the other hand, the mean Δ (\pm SD) was 0 ± 8 (4 ± 10) m/s and the mean $|\Delta|$ (\pm SD) was 6 ± 5 (8 ± 7) m/s,
for the Rayleigh clear (Mie cloudy) configuration. The results for the Rayleigh clear configuration did not change much, and
only the statistical significance was slightly reduced, while the results worsened significantly for the Mie cloudy
475 configuration, especially the slope. In the vertically resolved study, no significant improvement of the agreement was seen
and in fact the RMSE significantly increased in all of the vertical intervals. When considering only the 5 new overpasses
(Table 2, row h), the results for the Rayleigh clear configuration were similar to the ones obtained before, while the results
for the Mie cloudy configuration worsened considerably. This analysis yielded the conclusion that Aeolus and radiosonde's
data has to be properly spatiotemporally collocated for the Mie cloudy configuration. However, spatiotemporal collocation
480 for the Rayleigh clear configuration was not so determinant.

Table 2. Statistical results of the comparison between Aeolus wind products and radiosonde measurements. For each cell, the upper result refers to the Rayleigh clear configuration, while the lower result refers to the Mie cloudy configuration. SD stands for standard deviation, while SE stands for standard error. Overpasses considered in (a) are not considered in (h), while overpasses considered in (a) and in (h) are jointly considered in (g)

	orbit	ground track max. dist. (km)	radiosonde time launch	bins	mean bins distance	slope	intercept (m/s)	R	Δ (m/s)	$ \Delta $ (m/s)
--	-------	------------------------------	------------------------	------	--------------------	-------	-----------------	---	----------------	------------------



(a)	ANX2.0	100	~ 30 min	188	75 ± 19	0.96 ± 0.04	0.3 ± 0.5	0.87	0 ± 7	6 ± 5
				43	72 ± 17	0.84 ± 0.09	3 ± 1	0.84	7 ± 10	10 ± 7
(b)	ANX2.0 ascen. mode			138	69 ± 20	0.96 ± 0.06	0.5 ± 0.7	0.80	0 ± 8	6 ± 5
		38	71 ± 17	0.67 ± 0.05	3 ± 1	0.91	7 ± 11	11 ± 7		
(c)	ANX2.0 descen. mode			50	92 ± 5	0.77 ± 0.10	-4 ± 2	0.74	0 ± 6	5 ± 4
				5	82 ± 7	-0.6 ± 1.4	-30 ± 20	0.25	0 ± 10	0 ± 7
(d)	ANX2.0	110	~ 30 min	267	84 ± 21	0.92 ± 0.03	-0.1 ± 0.5	0.88	0 ± 7	6 ± 5
				47	75 ± 17	0.81 ± 0.07	2 ± 1	0.85	7 ± 10	10 ± 7
(e)		120		279	85 ± 22	0.93 ± 0.04	0.1 ± 0.5	0.87	0 ± 8	6 ± 5
				53	79 ± 21	0.84 ± 0.07	2 ± 1	0.84	5 ± 10	9 ± 7
(f)		140		312	90 ± 25	0.93 ± 0.04	0.2 ± 0.4	0.87	0 ± 8	6 ± 5
				63	87 ± 27	0.79 ± 0.09	1 ± 1	0.76	4 ± 10	10 ± 7
(g)	ANX2.0	100	≤ 12 h (& ≤ 30 min)	329	77 ± 17	0.95 ± 0.04	-0.1 ± 0.5	0.81	0 ± 8	6 ± 5
					69	74 ± 15	0.58 ± 0.06	0.9 ± 0.7	0.78	4 ± 10
(h)			≤ 12 h & ≥ 30 min	141	81 ± 11	0.97 ± 0.09	-0.6 ± 0.9	0.68	-1 ± 9	7 ± 6
				26	77 ± 13	-0.1 ± 0.1	8 ± 2	0.14	-4 ± 4	4 ± 4

485

5 Conclusions

In this work, Aeolus HLOS wind speed products from the Rayleigh clear and Mie cloudy configurations have been statistically validated with spatiotemporally collocated ground-based Doppler lidar measurements and radiosoundings at the ACTRIS/AGORA station of Granada.

490 It was observed that the error estimate filtering is needed, especially to avoid biases introduced by SNR issues and improve the comparison between the satellite and the uplooking instrumentation. The 8 (4) m/s limit for the Rayleigh clear (Mie cloudy) configuration was proven to be effective.

When comparing Aeolus ANX4.5 (B10 and B11) products with the uninterrupted ground-based Doppler lidar measurements, Aeolus did not seem to systematically underestimate or overestimate the HLOS wind speed. The slope, intercept and Pearson correlation coefficient showed minor disagreements between the instruments. The ground-based
 495 Doppler lidar system proved its effectiveness for validating Aeolus measurements because of its continuous retrieval of wind information, but the instrument is limited by its vertical coverage, from which the results of the comparison are limited to altitudes lower than 3.0 km asl. The vertical coverage limitation was observed to emphasize during night-time or early morning overpasses, when the ABL height is lower and the region with enough backscattered signal is reduced (lower SNR).

500 This limitation is softened under cloudy conditions, when the backscattered signal rises (higher SNR). Additionally, it was observed that a more restricted or less restricted spatial collocation of Aeolus products did not significantly improve the comparison. Thus, the 100 km limit proposed by ESA is confirmed. Analogously, when a larger interval of ground-based



Doppler lidar measurements was averaged the agreement was also worsened for both configurations. When comparing Aeolus ANX2.0 (B12) products, the agreement significantly worsened, so cases before and after the orbit shift should not be analyzed together and should be addressed separately. Therefore, the Doppler lidar system could be used to successfully perform Cal/Val activities in regions such as Granada. However, it was proven that Aeolus and ground-based Doppler lidar measurements have to be well spatiotemporally collocated, as the comparison is limited to the ABL, where the wind conditions can vary significantly. When comparing Aeolus ANX2.0 (B12) products with radiosondes, the Rayleigh clear configuration did not seem to systematically overestimate or underestimate the HLOS wind speed, while the Mie cloudy configuration seemed to overestimate the HLOS wind speed. However, this positive difference might be associated with the larger distance between the Mie cloudy bins and the radiosondes and to the fact that cloud properties may vary significantly spatially. The slope, intercept and Pearson correlation coefficient showed an almost perfect agreement for the Rayleigh clear configuration, while the Mie cloudy configuration presented significant disagreements. In this case, the radiosondes' vertical coverage was not a handicap, as they reached up to 20 km asl, providing full coverage of Aeolus products. Additionally, it was proven that radiosondes spatial and temporal collocation is really important for the Mie cloudy configuration, and not significantly for the Rayleigh clear configuration. Therefore, radiosondes could be used to successfully perform Cal/Val activities in regions such as Granada.

Both instruments were successful when validating Aeolus products. The ground-based Doppler lidar system measured uninterruptedly but presented a vertical coverage limitation, while the radiosondes were scarcer but provided a full vertical coverage of Aeolus profiles. A combination of both instruments could provide a full assessment of Aeolus wind products performance. Aeolus products were proven to provide reliable wind estimations. In the case of the Rayleigh clear configuration, the vertical coverage was significantly larger, providing information from the surface (with significantly low SNR) to 20 km. The Mie cloudy configuration provided fewer wind estimations, which were restricted to the presence of, generally, clouds. However, by default the Mie channel presents higher SNR than the Rayleigh channel. Regarding the comparison performed, the Rayleigh clear estimations were validated and proven to be valid estimations, while the Mie cloudy estimations were also validated but because of the distance between the instruments the differences obtained could be related to cloud properties differences rather than real Aeolus' biases. Additionally, for both channels the differences reported exceeded the systematic errors limit set by the mission requirements of 0.7 m/s. From a vertically resolved approach of the comparison, Aeolus presented larger RMSE for the lowermost measurements, especially for the Rayleigh clear configuration (lower SNR), while the RMSE was slightly reduced with the altitude.

Code availability

The code is not publicly accessible; however, readers may contact Jesús Abril-Gago (jabrilgago@ugr.es) and Juan Luis Guerrero-Rascado (rascado@ugr.es) for further information.



Data availability

535 Aeolus data files are available from the ESA Aeolus Online Dissemination System (<https://aeolus-ds.eo.esa.int>, ESA, 2022). The accessibility of these files is limited based on the ESA criteria. Readers may contact Jesús Abril-Gago (jabrilgago@ugr.es) and Juan Luis Guerrero-Rascado (rascado@ugr.es) for access to Doppler lidar and radiosonde measurements.

Author contributions

540 JAG and JLGR conceptualized the study, developed the methodology, and carried out the investigation and validation. JAG, JLGR, POA, DBP, JAM, JABA, MJGM, FNG, LAA and IFM were responsible for data curation and undertook the formal analysis. JAG and JLGR wrote the original draft of the paper, and JAG, JLGR, POA, DBP, JAM, JABA, MJGM, FNG, LAA and IFM reviewed and edited the paper.

Competing interests

545 The contact author has declared that neither they nor their co-authors have any competing interests.

Acknowledgments

This research was funded by the Spanish Ministry of Science and Innovation through the projects PID2020.117825GB.C21 and PID2020-120015RB-I00; by the Regional Government of Andalusia through the projects A-RNM-430-UGR20, P18-RT-3820, and P20-00136, and by the Horizon 2020 Framework Programme of the European Union, grant number 654109.

550 This research was partially supported by the Scientific Units of Excellence Program (grant no. UCE-PP2017-02). Jesús Abril-Gago received funding from the Spanish Ministry of Research and Innovation (Agencia Estatal de Investigación), grant PRE2021-097060 (co-funded by the European Social Fund Plus). Pablo Ortiz-Amezcu received funding from Fundación Ramón Areces through grant ‘Ampliación de estudios en el extranjero en Ciencias de la Vida y de la Materia. XXXII Convocatoria’ and from Polish National Science Centre (NCN) through project 2021/40/C/ST10/00023 of

555 programme SONATINA 5. Francisco Navas-Guzmán received funding from the Ramón y Cajal program (ref. RYC2019-027519-I) of the Spanish Ministry of Science and Innovation. The authors gratefully acknowledge the FEDER program for the instrumentation used in this study, which is part of the ‘Laboratorio Singular de Tecnologías Avanzadas Observatorio Global de la Atmósfera (AGORA), supported by the University of Granada, and the COST Action PROBE (CA18235), supported by COST (European Cooperation in Science and Technology) for the exchange of expertise.



560 References

- Miller, B. B. and Carter, C.: The test article, *J. Sci. Res.*, 12, 135–147, doi:10.1234/56789, 2015.
- Smith, A. A., Carter, C., and Miller, B. B.: More test articles, *J. Adv. Res.*, 35, 13–28, doi:10.2345/67890, 2014.
- Abril-Gago, J., Guerrero-Rascado, J. L., Costa, M. J., Bravo-Aranda, J. A., Sicard, M., Bermejo-Pantaleón, D., Bortoli, D., Granados-Muñoz, M. J., Rodríguez-Gómez, A., Muñoz-Porcar, C., Comerón, A., Ortiz-Amezcuca, P., Salgueiro, V.,
565 Jiménez-Martín, M. M., and Alados-Arboledas, L.: Statistical validation of Aeolus L2A particle backscatter coefficient retrievals over ACTRIS/EARLINET stations on the Iberian Peninsula, *Atmos. Chem. Phys.*, 22, 1425–1451, https://doi.org/10.5194/acp-22-1425-2022, 2022
- Alados-Arboledas, L., Müller, D., Guerrero-Rascado, J. L., Navas-Guzmán, F., Pérez-Ramírez, D., and Olmo, F. J.:
570 Optical and microphysical properties of fresh biomass burning aerosol retrieved by Raman lidar, and star-and sun-photometry, *Geophys. Res. Lett.*, 38, L01807, https://doi.org/10.1029/2010GL045999, 2011.
- Andersson, E.: Statement of Guidance for Global Numerical Weather Prediction (NWP), World Meteorological Organisation, https://docplayer.net/194586713-Statement-of-guidance-for-global-numerical-weatherprediction-nwp.html (last access: 17 October 2022), 2018.
- Baars, H., Herzog, A., Heese, B., Ohneiser, K., Hanbuch, K., Hofer, J., Yin, Z., Engelmann, R., and Wandinger, U.:
575 Validation of Aeolus wind products above the Atlantic Ocean, *Atmos. Meas. Tech.*, 13, 6007–6024, https://doi.org/10.5194/amt-13-6007-2020, 2020.
- Baars, H., Radenz, M., Floutsi, A. A., Engelmann, R., Althausen, D., Heese, B., Ansmann, A., Flament, T., Dabas, A., Trajon, D., Reitebuch, O., Bley, S., and Wandinger, U.: Californian Wildfire Smoke Over Europe: A First Example of the Aerosol Observing Capabilities of Aeolus Compared to Ground-Based Lidar, *Geophys. Res. Lett.*, 48, e2020GL092194,
580 https://doi.org/10.1029/2020GL092194, 2021.
- Bedka, K. M., Nehrir, A. R., Kavaya, M., Barton-Grimley, R., Beaubien, M., Carroll, B., Collins, J., Cooney, J., Emmitt, G. D., Greco, S., Kooi, S., Lee, T., Liu, Z., Rodier, S., and Skofronick-Jackson, G.: Airborne lidar observations of wind, water vapor, and aerosol profiles during the NASA Aeolus calibration and validation (Cal/Val) test flight campaign, *Atmos. Meas. Tech.*, 14, 4305–4334, https://doi.org/10.5194/amt-14-4305-2021, 2021.
- 585 Bedoya-Velásquez, A. E., Navas-Guzmán, F., Granados-Muñoz, M. J., Titos, G., Román, R., Casquero-Vera, J. A., Ortiz-Amezcuca, P., Benavent-Oltra, J. A., de Arruda Moreira, G., Montilla-Rosero, E., Hoyos, C. D., Artiñano, B., Coz, E., Olmo-Reyes, F. J., Alados-Arboledas, L., and Guerrero-Rascado, J. L.: Hygroscopic growth study in the framework of EARLINET during the SLOPE I campaign: synergy of remote sensing and in situ instrumentation, *Atmos. Chem. Phys.*, 18, 7001–7017, https://doi.org/10.5194/acp-18-7001-2018, 2018.
- 590 Bedoya-Velásquez, A. E., Navas-Guzmán, F., de Arruda Moreira, G., Román, R., Cazorla, A., Ortiz-Amezcuca, P., Benavent-Oltra, J. A., Alados-Arboledas, L., Olmo-Reyes, F. J., Foyo-Moreno, I., Montilla-Rosero, E., Hoyos, C. D., and



- Guerrero-Rascado, J. L.: Seasonal analysis of the atmosphere during five years by using microwave radiometry over a mid-latitude site, *Atmospheric Research*, 218, 78–89, <https://doi.org/10.1016/j.atmosres.2018.11.014>, 2019a.
- Bedoya-Velásquez, A. E., Titos, G., Bravo-Aranda, J. A., Haefelin, M., Favez, O., Petit, J.-E., Casquero-Vera, J. A.,
595 Olmo-Reyes, F. J., Montilla-Rosero, E., Hoyos, C. D., Alados-Arboledas, L., and Guerrero-Rascado, J. L.: Long-term aerosol optical hygroscopicity study at the ACTRIS SIRTAs observatory: synergy between ceilometer and in situ measurements, *Atmos. Chem. Phys.*, 19, 7883–7896, <https://doi.org/10.5194/acp-19-7883-2019>, 2019b.
- Belova, E., Kirkwood, S., Voelger, P., Chatterjee, S., Satheesan, K., Hagelin, S., Lindskog, M., and Körnich, H.: Validation of Aeolus winds using ground-based radars in Antarctica and in northern Sweden, *Atmos. Meas. Tech.*, 14, 5415–
600 5428, <https://doi.org/10.5194/amt-14-5415-2021>, 2021.
- Bosque Maurel, J.: El clima de Granada, *Estud. Geográficos*, 20, 145–147, <https://www.proquest.com/docview/1304223170?pq-origsite=gscholar&fromopenview=true&imgSeq=1> (last access: 17 October 2022), 1959.
- Browning, K. A., and Wexler, R.: The determination of kinematic properties of a wind field using Doppler radar. *J. Appl. Meteor.*, 7, 105–113. [https://doi.org/10.1175/1520-0450\(1968\)007<0105:TDOKPO>2.0.CO;2](https://doi.org/10.1175/1520-0450(1968)007<0105:TDOKPO>2.0.CO;2), 1968.
- Bravo-Aranda, J. A., Titos, G., Granados-Muñoz, M. J., Guerrero-Rascado, J. L., Navas-Guzmán, F., Valenzuela, A., Lyamani, H., Olmo, F. J., Andrey, J., and Alados-Arboledas, L.: Study of mineral dust entrainment in the planetary boundary layer by lidar depolarisation technique, *Tellus B*, 67, 26180, <https://doi.org/10.3402/tellusb.v67.26180>, 2015.
- Cariñanos, P., Foyo-Moreno, I., Alados, I., Guerrero-Rascado, J. L., Ruiz-Peñuela, S., Titos, G., Cazorla, A., Alados-Arboledas, L., and Díaz de la Guardia, C.: Bioaerosols in urban environments: Trends and interactions with pollutants and meteorological variables based on quasi-climatological series, *J. Environ. Manage.*, 282, 111963, <https://doi.org/10.1016/j.jenvman.2021.111963>, 2021.
- Cariñanos, P., Guerrero-Rascado, J. L., Valle, A. M., Cazorla, A., Titos, G., Foyo-Moreno, I., Alados-Arboledas, L., and Díaz de la Guardia, C.: Assessing pollen extreme events over a Mediterranean site: role of local surface meteorology, *Atmospheric Environment*, 272, 118928, 1–13, <https://doi.org/10.1016/j.atmosenv.2021.118928>, 2022.
- Casquero-Vera, J. A., Lyamani, H., Titos, G., Minguillón, M.C., Dada, L., Alastuey, A., Querol, X., Petäjä, T., Olmo, F. J., and Alados-Arboledas, L.: Quantifying traffic, biomass burning and secondary source contributions to atmospheric particle number concentrations at urban and suburban sites, *Science of the Total Environment*, 768, 145282, <https://doi.org/10.1016/j.scitotenv.2021.145282>, 2021.
- 620 Cazorla, A., Casquero-Vera, J. A., Román, R., Guerrero-Rascado, J. L., Toledano, C., Cachorro, V. E., Orza, J. A. G., Cancillo, M. L., Serrano, A., Titos, G., Pandolfi, M., Alastuey, A., Hanrieder, N., and Alados-Arboledas, L.: Near-real-time processing of a ceilometer network assisted with sun-photometer data: monitoring a dust outbreak over the Iberian Peninsula, *Atmos. Chem. Phys.*, 17, 11861–11876, <https://doi.org/10.5194/acp-17-11861-2017>, 2017.



Chen, S., Cao, R., Xie, Y., Zhang, Y., Tan, W., Chen, H., Guo, P., and Zhao, P.: Study of the seasonal variation in
625 Aeolus wind product performance over China using ERA5 and radiosonde data, *Atmos. Chem. Phys.*, 21, 11489–11504,
<https://doi.org/10.5194/acp-21-11489-2021>, 2021.

de Arruda Moreira, G., Guerrero-Rascado, J. L., Bravo-Aranda, J. A., Benavent-Oltra, J. A., Ortiz-Amezcuca, P., Román,
R., Bedoya-Velásquez, A. E., Landulfo, E., and Alados-Arboledas, L.: Study of the planetary boundary layer by microwave
radiometer, elastic lidar and Doppler lidar estimations in Southern Iberian Peninsula, *Atmospheric Research*, 213, 185-195,
630 <https://doi.org/10.1016/j.atmosres.2018.06.007>, 2018.

European Space Agency (ESA): ADM-Aeolus Science Report, ESA SP-1311, 121 pp.,
<https://esamultimedia.esa.int/multimedia/publications/SP-1311/SP-1311.pdf> (last access: 17 October 2022), 2008.

Fehr, T., Piña, A., Amiridis, V., Baars, H., von Bismarck, J., Borne, M., Cazenave, Q., Chen, S., Flamant, C., Gaetani,
M., Knipperz, P., Koopman, R., Lemmerz, C., Marinou, E., Mocnik, G., Parrinello, T., Reitebuch, O., Skofronick-Jackson,
635 G., Straume, A. G., and Zenk, C.: The Joint Aeolus Tropical Atlantic Campaign – First Results for Aeolus
Calibration/Validation and Science in the Tropics, *ESA Atmospheric Science Conference (2021)*, Online, 22 – 26 November
2021, <https://atmos2021.esa.int/agenda/> (last access: 17 October 2022), 2021.

Fehr, T.: The Joint Aeolus Tropical Atlantic Campaign 2021, Aeolus 3rd Anniversary Conference, Taormina, Italy, 28
March – 1 April 2022, <https://www.aeolus3years.org/detailed-agenda> (last access: 17 October 2022), 2022.

640 Feofilov, A. G., Chepfer, H., Noël, V., Guzman, R., Gindre, C., Ma, P.-L., Chiriaco, M.: Comparison of scattering ratio
profiles retrieved from ALADIN/Aeolus and CALIOP/CALIPSO observations and preliminary estimates of cloud fraction
profiles, *Atmos. Meas. Tech.*, 15, 1055–1074, <https://doi.org/10.5194/amt-15-1055-2022>, 2022.

Fernández, A. J., Sicard, M., Costa, M. J., Guerrero-Rascado, J. L., Gómez-Amo, J. L., Molero, F., Barragán, R., Basart,
S., Bortoli, D., Bedoya-Velásquez, A. E., Utrillas, M. P., Salvador, P., Granados-Muñoz, M. J., Potes, M., Ortiz-Amezcuca,
645 P., Martínez-Lozano, J. A., Artíñano, B., Muñoz-Porcar, C., Salgado, R., Román, R., Rocadenbosch, F., Salgueiro, V.,
Benavent-Oltra, J. A., Rodríguez-Gómez, A., Alados-Arboledas, L., Comerón, A., and Pujadas, M.: Extreme, wintertime
Saharan dust intrusion in the Iberian Peninsula: Lidar monitoring and evaluation of dust forecast models during the February
2017 event, *Atmos. Res.*, 228, 223–241, <https://doi.org/10.1016/j.atmosres.2019.06.007>, 2019.

Flamant, P. H., Lever, V., Martinet, P., Flament, T., Cuesta, J., Dabas, A., Olivier, M., and Huber, D.: ADM-Aeolus L2A
650 Algorithm Theoretical Baseline Document Particle spin-off products, ESA, reference: AE-TN-IPSL-GS-001, available at:
<https://earth.esa.int/eogateway/documents/20142/37627/Aeolus-L2A-Algorithm-Theoretical-Baseline-Document> (last
access: 17 October 2022), 2020.

Flament, T., Trapon, D., Lacour, A., Dabas, A., Ehlers, F., and Huber, D.: Aeolus L2A aerosol optical properties product:
standard correct algorithm and Mie correct algorithm, *Atmos. Meas. Tech.*, 14, 7851–7871, <https://doi.org/10.5194/amt-14-7851-2021>,
655 7851-2021, 2021.

Gkikas, A., Gialitaki, A., Biniotoglou, I., Marinou, E., Tschla, M., Siomos, N., Paschou, P., Kampouri, A., Voudouri, K.
A., Proestakis, E., Mylonaki, M., Papanikolaou, C.-A., Michailidis, K., Baars, H., Straume, A. G., Balis, D., Papayannis, A.,



- Parrinello, T., and Amiridis, V.: First assessment of Aeolus L2A particle backscatter coefficient retrievals in the Eastern Mediterranean, *Atmos. Meas. Tech. Discuss.* [preprint], <https://doi.org/10.5194/amt-2022-205>, in review, 2022.
- 660 Granados-Muñoz, M. J., Navas-Guzmán, F., Bravo-Aranda, J. A., Guerrero-Rascado, J. L., Lyamani, H., Fernández-Gálvez, J., and Alados-Arboledas, L.: Automatic determination of the planetary boundary layer height using lidar: One-year analysis over southeastern Spain, *J. Geophys. Res.*, 117, D18208, <https://doi.org/10.1029/2012JD017524>, 2012.
- Granados-Muñoz, M. J., Bravo-Aranda, J. A., Baumgardner, D., Guerrero-Rascado, J. L., Pérez-Ramírez, D., Navas-Guzmán, F., Veselovskii, I., Lyamani, H., Valenzuela, A., Olmo, F. J., Titos, G., Andrey, J., Chaikovsky, A., Dubovik, O.,
665 Gil-Ojeda, M., and Alados-Arboledas, L.: A comparative study of aerosol microphysical properties retrieved from ground-based remote sensing and aircraft in situ measurements during a Saharan dust event, *Atmos. Meas. Tech.*, 9, 1113–1133, <https://doi.org/10.5194/amt-9-1113-2016>, 2016.
- Guerrero-Rascado, J. L., Ruiz, B., and Alados-Arboledas, L.: Multispectral Lidar characterization of the vertical structure of Saharan dust aerosol over southern Spain, *Atmos. Environ.*, 42, 2668–2681,
670 <https://doi.org/10.1016/j.atmosenv.2007.12.062>, 2008.
- Guerrero-Rascado, J. L., Olmo, F. J., Avilés-Rodríguez, I., Navas-Guzmán, F., Pérez-Ramírez, D., Lyamani, H., and Alados-Arboledas, L.: Extreme Saharan dust event over the southern Iberian Peninsula in september 2007: active and passive remote sensing from surface and satellite, *Atmos. Chem. Phys.*, 9, 8453–8469, <https://doi.org/10.5194/acp-9-8453-2009>, 2009.
- 675 Guo, J., Liu, B., Gong, W., Shi, L., Zhang, Y., Ma, Y., Zhang, J., Chen, T., Bai, K., Stoffelen, A., de Leeuw, G., and Xu, X.: Technical note: First comparison of wind observations from ESA's satellite mission Aeolus and ground-based radar wind profiler network of China, *Atmos. Chem. Phys.*, 21, 2945–2958, <https://doi.org/10.5194/acp-21-2945-2021>, 2021.
- Illingworth, A. J., Hogan, R. J., O'Connor, E. J., Bouniol, D., Brooks, M. E., Delanoé, J., Donovan, D. P., Eastment, J. D., Gaussiat, N., Goddard, J. W. F., Haeffelin, M., Baltink, H. K., Krasnov, O. A., Pelon, J., Piriou, J.-M., Protat, A.,
680 Russchenberg, H. W. J., Seifert, A., Tompkins, A. M., van Zadelhoff, G.-J., Vinit, F., Willén, U., Wilson, D. R., and Wrench, C. L.: Cloudnet, *Bulletin of the American Meteorological Society*, 88(6), 883–898, <https://doi.org/10.1175/BAMS-88-6-883>, 2007.
- Ingmann, P. and Straume, A. G.: ADM-Aeolus Mission Requirements Document, ESA, reference: AE-RP-ESA-SY-001 EOP-SM/2047, available at: <https://earth.esa.int/eogateway/documents/20142/1564626/Aeolus-Mission-Requirements.pdf>
685 (last access: 17 October 2022), 2016.
- Iwai, H., Aoki, M., Oshiro, M., and Ishii, S.: Validation of Aeolus Level 2B wind products using wind profilers, groundbased Doppler wind lidars, and radiosondes in Japan, *Atmos. Meas. Tech.*, 14, 7255–7275, <https://doi.org/10.5194/amt-14-7255-2021>, 2021.
- Khaykin, S. M., Hauchecorne, A., Wing, R., Keckhut, P., Godin-Beekmann, S., Porteneuve, J., Mariscal, J.-F., and
690 Schmitt, J.: Doppler lidar at Observatoire de Haute-Provence for wind profiling up to 75 km altitude: performance evaluation and observations, *Atmos. Meas. Tech.*, 13, 1501–1516, <https://doi.org/10.5194/amt-13-1501-2020>, 2020.



- López-Cayuela, M.-Á., Córdoba-Jabonero, C., Bermejo-Pantaleón, D., Sicard, M., Salgueiro, V., Molero, F., Carvajal-Pérez, C. V., Granados-Muñoz, M. J., Comerón, A., Couto, F. T., Barragán, R., Zorzano, M.-P., Bravo-Aranda, J. A., Muñoz-Pocar, C., Costa, M. J., Artíñano, B., Rodríguez-Gómez, A., Bortoli, D., Pujadas, M., Abril-Gago, J., Alados-Arboledas, L., and Guerrero-Rascado, J. L.: Vertical characterization of the dust fine and coarse particles during an intense Saharan dust outbreak over the Iberian Peninsula in springtime 2021, *Atmos. Chem. Phys. Discuss.* [preprint], <https://doi.org/10.5194/acp-2022-380>, in review, 2022.
- Lux, O., Lemmerz, C., Weiler, F., Marksteiner, U., Witschas, B., Rahm, S., Geiß, A., and Reitebuch, O.: Intercomparison of wind observations from the European Space Agency's Aeolus satellite mission and the ALADIN Airborne Demonstrator, *Atmos. Meas. Tech.*, 13, 2075–2097, <https://doi.org/10.5194/amt-13-2075-2020>, 2020.
- Lux, O., Lemmerz, C., Weiler, F., Marksteiner, U., Witschas, B., Rahm, S., Geiß, A., Schäfler, A., and Reitebuch, O.: Retrieval improvements for the ALADIN Airborne Demonstrator in support of the Aeolus wind product validation, *Atmos. Meas. Tech.*, 15, 1303–1331, <https://doi.org/10.5194/amt-15-1303-2022>, 2022a.
- Lux, O., Witschas, B., Geiß, A., Lemmerz, C., Weiler, F., Marksteiner, U., Rahm, S., Schäfler, A., and Reitebuch, O.: Quality control and error assessment of the Aeolus L2B wind results from the Joint Aeolus Tropical Atlantic Campaign, *Atmos. Meas. Tech. Discuss.* [preprint], <https://doi.org/10.5194/amt-2022-223>, in review, 2022b.
- Lyamani, H., Olmo, F. J., and Alados-Arboledas, L.: Physical and optical properties of aerosols over an urban location in Spain: seasonal and diurnal variability, *Atmos. Chem. Phys.*, 10, 239–254, <https://doi.org/10.5194/acp-10-239-2010>, 2010.
- Lyamani, H., Fernández-Gálvez, J., Pérez-Ramírez, D., Valenzuela, A., Antón, M., Alados, I., Titos, G., Olmo, F. J., and Alados-Arboledas, L.: Aerosol properties over two urban sites in South Spain during an extended stagnation episode in winter season, *Atmos. Environ.*, 62, 424–432, <https://doi.org/10.1016/j.atmosenv.2012.08.050>, 2012.
- Martin, A., Weissmann, M., Reitebuch, O., Rennie, M., Geiß, A., and Cress, A.: Validation of Aeolus winds using radiosonde observations and numerical weather prediction model equivalents, *Atmos. Meas. Tech.*, 14, 2167–2183, <https://doi.org/10.5194/amt-14-2167-2021>, 2021.
- Montávez, J.P., Rodríguez, A., and Jiménez, J.I.: A study of the urban heat island of Granada. *Int. J. Climatol.*, 20, 899–911, [https://doi.org/10.1002/1097-0088\(20000630\)20:8%3C899::AID-JOC433%3E3.0.CO;2-I](https://doi.org/10.1002/1097-0088(20000630)20:8%3C899::AID-JOC433%3E3.0.CO;2-I), 2000.
- Myhre, G., Shindell, D., Bréon, F. M., Collins, W., Fuglestedt, J., Huang, J., Koch, D., Lamarque, J. F., Lee, D., Mendoza, B., Nakajima, T., Robock, A., Stephens, G., Takemura, T., and Zhang, H.: Anthropogenic and natural radiative forcing. In: *Climate Change 2013: The Physical Science Basis. Contribution of Working Group I to the Fifth Assessment Report of the Intergovernmental Panel on Climate Change*, edited by: Stocker, T. F., Qin, D., Plattner, G.-K., Tignor, M., Allen, S. K., Boschung, J., Nauels, A., Xia, Y., Bex, V., and Midgley, P. M., 9781107057, Cambridge University Press, 659–740, <https://doi.org/10.1017/CBO9781107415324.018>, 2013.
- Navas-Guzmán, F., Bravo-Aranda, J. A., Guerrero-Rascado, J. L., Granados-Muñoz, M. J., and Alados-Arboledas, L.: Statistical analysis of aerosol optical properties retrieved by Raman lidar over Southeastern Spain, *Tellus B: Chemical and Physical Meteorology*, 65:1, <https://doi.org/10.3402/tellusb.v65i0.21234>, 2013.



- Navas-Guzmán, F., Fernández-Gálvez, J., Granados-Muñoz, M. J., Guerrero-Rascado, J. L., Bravo-Aranda, J. A., and Alados-Arboledas, L.: Tropospheric water vapour and relative humidity profiles from lidar and microwave radiometry, *Atmos. Meas. Tech.*, 7, 1201–1211, <https://doi.org/10.5194/amt-7-1201-2014>, 2014.
- 730 Ortiz-Amezcuca, P., Guerrero-Rascado, J. L., Granados-Muñoz, M. J., Bravo-Aranda, J. A., and Alados-Arboledas, L.: Characterization of atmospheric aerosols for a long range transport of biomass burning particles from canadian forest fires over the southern iberian peninsula in july 2013, *Optica Pura y Aplicada*, 47, 43– 49, <https://doi.org/10.7149/OPA.47.1.43>, 2014.
- Ortiz-Amezcuca, P., Guerrero-Rascado, J. L., Granados-Muñoz, M. J., Benavent-Oltra, J. A., Böckmann, C., Samaras, S., Stachlewska, I. S., Janicka, Ł., Baars, H., Bohlmann, S., and Alados-Arboledas, L.: Microphysical characterization of long-range transported biomass burning particles from North America at three EARLINET stations, *Atmos. Chem. Phys.*, 17, 5931–5946, <https://doi.org/10.5194/acp-17-5931-2017>, 2017.
- 735 Ortiz-Amezcuca, P., Martínez-Herrera, A., Manninen, A. J., Pentikäinen, P. P., O’Connor, E. J., Guerrero-Rascado, J. L., and Alados-Arboledas, L.: Wind and Turbulence Statistics in the Urban Boundary Layer over a Mountain–Valley System in Granada, Spain, *Remote Sensing*, 14, 2321, <https://doi.org/10.3390/rs14102321>, 2022a.
- 740 Ortiz-Amezcuca, P., Andújar-Maqueda, J., Manninen, A. J., Pentikäinen, P., O’Connor, E. J., Stachlewska, I. S., de Arruda Moreira, G., Benavent-Oltra, J. A., Casquero-Vera, J. A., Poczta, P., Wang, D., Harenda, K. M., Chojnicki, B. H., Szczepanik, D. M., Janicka, Ł., Schüttemeyer, D., Alados-Arboledas, L., and Guerrero-Rascado, J. L.: Dynamics of the Atmospheric Boundary Layer over two middle-latitude rural sites with Doppler lidar, *Atmospheric Research*, 280, 106434, <https://doi.org/10.1016/j.atmosres.2022.106434>, 2022b.
- 745 Pearson, G., Davies, F., and Collier, C.: An analysis of the performance of the UFAM pulsed Doppler lidar for observing the boundary layer, *J. Atmos. Ocean. Technol.*, 26, 240–250, <https://doi.org/10.1175/2008JTECHA1128.1>, 2009.
- Pentikäinen, P., O’Connor, E. J., Manninen, A. J., and Ortiz-Amezcuca, P.: Methodology for deriving the telescope focus function and its uncertainty for a heterodyne pulsed Doppler lidar, *Atmos. Meas. Tech.*, 13, 2849–2863, <https://doi.org/10.5194/amt-13-2849-2020>, 2020.
- 750 Ratynski, M., Khaykin, S., Hauchecorne, A., Wing, R., Cammas, J.-P., Hello, Y., and Keckhut, P.: Validation of Aeolus wind profiles using ground-based lidar and radiosonde observations at La Réunion Island and the Observatoire de Haute Provence, *EGUsphere* [preprint], <https://doi.org/10.5194/egusphere-2022-822>, 2022.
- Reitebuch, O.: The Spaceborne Wind Lidar Mission ADM-Aeolus, in: *Atmospheric physics: Background, methods, trends*, edited by: Schumann, U., *Research Topics in Aerospace*, Springer, Berlin, London, 815–827, 2012.
- 755 Reitebuch, O., Huber, D., and Nikolaus, I.: ADM-Aeolus Algorithm Theoretical Basis Document (ATBD) Level-1B Products, AE-RP-DLR-L1B-001, v. 4.4, 117 pp, 2008.
- Rennie, M., and Isaksen, L.: The NWP impact of Aeolus Level2B winds at ECMWF, *Technical Memorandum*, ECMWF, <https://doi.org/10.21957/alift7mhr>, 2020.



- Rennie, M., Tan, D., Andersson, E., Poli, P., Dabas, A., De Kloe, J., Marseille, G.-J., and Stoffelen, A.: Aeolus Level-2B
760 Algorithm Theoretical Basis Document (Mathematical Description of the Aeolus L2B Processor), AED-SD-ECMWF-L2B-
038, V. 3.4, 124 pp., ECMWF, <https://earth.esa.int/eogateway/documents/20142/37627/Aeolus-L2B-Algorithm-ATBD.pdf>
(last access: 17 October 2022), 2020.
- Rennie, M. P., Isaksen, L., Weiler, F., Kloe, J., Kanitz, T., and Reitebuch, O.: The impact of Aeolus wind retrievals in
ECMWF global weather forecasts, *Q. J. R. Meteorol. Soc.*, 147, 3555–3586, <https://doi.org/10.1002/qj.4142>, 2021.
- 765 Sicard, M., Granados-Muñoz, M. J., Alados-Arboledas, L., Barragán, R., Bedoya-Velásquez, A. E., Benavent-Oltra, J.
A., Bortoli, D., Comerón, A., Córdoba-Jabonero, C., Costa, M. J., del Águila, A., Fernández, A. J., Guerrero-Rascado, J. L.,
Jorba, O., Molero, F., Muñoz-Porcar, C., Ortiz-Amezcuca, P., Papagiannopoulos, N., Potes, M., Pujadas, M., Rocadenbosch,
F., Rodríguez-Gómez, A., Román, R., Salgado, R., Salgueiro, V., Sola, Y., and Yela, M.: Ground/space, passive/active
remote sensing observations coupled with particle dispersion modelling to understand the inter-continental transport of
770 wildfire smoke plumes, *Remote Sens. Environ.*, 232, 111294, <https://doi.org/10.1016/j.rse.2019.111294>, 2019.
- Stocker, T. F., Qin, D., Plattner, G.-K., Tignor, M., Allen, S. K., Boschung, J., Nauels, A., Xia, Y., Bex, V., and Midgley,
P. M. (Eds.): *Climate Change 2013: The Physical Science Basis. Contribution of Working Group I to the Fifth Assessment
Report of the Intergovernmental Panel on Climate Change*, Cambridge University Press, 1535 pp., available at:
https://www.ipcc.ch/site/assets/uploads/2018/03/WG1AR5_SummaryVolume_FINAL.pdf (last access: 17 October 2022),
775 2013.
- Stoffelen, A., Benedetti, A., Borde, R., Dabas, A., Flamant, P., Forsythe, M., Hardesty, M., Isaksen, L., Källén, E.,
Körnich, H., Lee, T., Reitebuch, O., Rennie, M., Riishøjgaard, L.-P., Schyberg, H., Straume, A. G., and Vaughan, M.: Wind
Profile Satellite Observation Requirements and Capabilities, *B. Am. Meteorol. Soc.*, 101, E2005-E2021,
<https://doi.org/10.1175/BAMS-D-18-0202.1>, 2020.
- 780 Straume, A. G., Schuettmeyer, D., Von Bismarck, J., Kanitz, T., and Fehr, T.: Aeolus Scientific Calibration and
Validation Implementation Plan, available at: [https://earth.esa.int/eogateway/documents/20142/1564626/Aeolus-Scientific-
CAL-VAL-Implementation-Plan.pdf](https://earth.esa.int/eogateway/documents/20142/1564626/Aeolus-Scientific-CAL-VAL-Implementation-Plan.pdf) (last access: 17 October 2022), 2019.
- Straume, A. G., Rennie, M., Isaksen, L., Kloe, J. de, Marseille, G.-J., Stoffelen, A., Flament, T., Stieglitz, H., Dabas, A.,
Huber, D., Reitebuch, O., Lemmerz, C., Lux, O., Marksteiner, U., Weiler, F., Witschas, B., Meringer, M., Schmidt, K.,
785 Nikolaus, I., Geiss, A., Flamant, P., Kanitz, T., Wernham, D., von Bismarck, J., Bley, S., Fehr, T., Floberghagen, R., and
Parinello, T.: ESA's SpaceBased Doppler Wind Lidar Mission Aeolus – First Wind and Aerosol Product Assessment
Results, *EPJ Web Conf.*, 237, 1007, <https://doi.org/10.1051/epjconf/202023701007>, 2020.
- Šavli, M., de Kloe, J., Marseille, G.-J., Rennie, M., Žagar, N., and Nils, W.: The prospects for increasing the horizontal
resolution of the Aeolus horizontal line-of-sight wind profiles, *Q. J. Roy. Meteor. Soc.*, 145, 3499–3515,
790 <https://doi.org/10.1002/qj.3634>, 2019.



- Tan, D. G. H., Rennie, M., Andersson, E., Poli, P., Dabas, A., de Kloe, J., Marseille, G.-J., and Stoffelen, A.: Aeolus Level2B Algorithm Theoretical Basis Document (Mathematical Description of the Aeolus Level-2B Processor), AE-TN-ECMWFL2BP-0023, v. 3.0, 109 pp, 2017.
- Vaughan, G., Wareing, D., Thomas, L., and Mitev, V.: Humidity measurements in the free troposphere using Raman backscatter. *Q. J. R. Meteorol. Soc.* 114, 1471–1484, 1988.
- Viedma Muñoz, M.: Análisis de las direcciones de los vientos en Andalucía, *Nimbus*, 1, 153–168, [http://repositorio.ual.es/bitstream/handle/10835/1493/199675\[1\].pdf?sequence=1](http://repositorio.ual.es/bitstream/handle/10835/1493/199675[1].pdf?sequence=1) (last access: 17 October 2022), 1998.
- von Bismarck, J.: AEOLUS Status Update, International Laser Radar Conference (30th ILRC), 2022.
- Witschas, B., Lemmerz, C., Geiß, A., Lux, O., Marksteiner, U., Rahm, S., Reitebuch, O., and Weiler, F.: First validation of Aeolus wind observations by airborne Doppler wind lidar measurements, *Atmos. Meas. Tech.*, 13, 2381–2396, <https://doi.org/10.5194/amt-13-2381-2020>, 2020.
- Witschas, B., Lemmerz, C., Geiß, A., Lux, O., Marksteiner, U., Rahm, S., Reitebuch, O., Schäfler, A., and Weiler, F.: Validation of the Aeolus L2B wind product with airborne wind lidar measurements in the polar North Atlantic region and in the tropics, *Atmos. Meas. Tech. Discuss.* [preprint], <https://doi.org/10.5194/amt-2022-233>, in review, 2022.
- Weiler, F., Kanitz, T., Wernham, D., Rennie, M., Huber, D., Schillinger, M., Saint-Pe, O., Bell, R., Parrinello, T., and Reitebuch, O.: Characterization of dark current signal measurements of the ACCDs used on board the Aeolus satellite, *Atmos. Meas. Tech.*, 14, 5153–5177, <https://doi.org/10.5194/amt14-5153-2021>, 2021a.
- Weiler, F., Rennie, M., Kanitz, T., Isaksen, L., Checa, E., de Kloe, J., Okunde, N., and Reitebuch, O.: Correction of wind bias for the lidar on board Aeolus using telescope temperatures, *Atmos. Meas. Tech.*, 14, 7167–7185, <https://doi.org/10.5194/amt14-7167-2021>, 2021b.
- World Meteorological Organization (WMO): Proceedings of the third WMO Workshop on the impact of various observing systems on numerical weather prediction, WMO, available at: https://library.wmo.int/doc_num.php?explnum_id=5409 (last access: 17 October 2022), 2004.
- Wu, S., Sun, K., Dai, G., Wang, X., Liu, X., Liu, B., Song, X., Reitebuch, O., Li, R., Yin, J., and Wang, X.: Inter-comparison of wind measurements in the atmospheric boundary layer and the lower troposphere with Aeolus and a ground-based coherent Doppler lidar network over China, *Atmos. Meas. Tech.*, 15, 131–148, <https://doi.org/10.5194/amt-15-131-2022>, 2022.